# Magnetic Braking and Protostellar Disk Formation: The Ideal MHD Limit

Richard R. Mellon[1] & Zhi-Yun Li[1]

## ABSTRACT

Magnetic fields are usually considered dynamically important in star formation when the dimensionless mass-to-flux ratio is close to, or less than, unity ($\lambda \lesssim 1$). We show that, in disk formation, the requirement is far less stringent. This conclusion is drawn from a set of 2D (axisymmetric) simulations of the collapse of rotating, singular isothermal cores magnetized to different degrees. We find that a weak field corresponding to $\lambda \sim 100$ can begin to disrupt the rotationally supported disk through magnetic braking, by creating regions of rapid, supersonic collapse in the disk. These regions are separated by one or more centrifugal barriers, where the rapid infall is temporarily halted. The number of centrifugal barriers increases with the mass-to-flux ratio $\lambda$. When $\lambda \gtrsim 100$, they merge together to form a more or less contiguous, rotationally supported disk. Even though the magnetic field in such a case is extremely weak on the scale of dense cores, it is amplified by collapse and differential rotation, to the extent that its pressure dominates the thermal pressure in both the disk and its surrounding region. For relatively strongly magnetized cores with $\lambda \lesssim 10$, the disk formation is suppressed completely, as found previously. A new feature is that the mass accretion is highly episodic, due to reconnection of the magnetic field lines accumulated near the center. For rotationally supported disks to appear during the protostellar mass accretion phase of star formation in dense cores with realistic field strengths, the powerful magnetic brake must be weakened, perhaps through nonideal MHD effects. Another possibility is to remove, through protostellar winds, the material that acts to brake the disk rotation. We discuss the possibility of observing a generic product of the magnetic braking, an extended circumstellar region that is supported by a combination of toroidal magnetic field and rotation — a "magnetogyrosphere" — interferometrically.

*Subject headings:* accretion disks — ISM: molecular clouds and magnetic fields — MHD — stars: formation

---

[1]Astronomy Department, University of Virginia, Charlottesville, VA 22904; rrm8p, zl4h@virginia.edu

## 1. Introduction

Disks are commonly observed around low-mass young stellar objects. They play a central role in star formation. It is generally believed that most of the mass of a Sun-like star is assembled through a disk (Shu, Adams, & Lizano 1987). The disks may also be responsible for regulating the rotation rates of young stars, through disk-stellar magnetosphere interaction (Königl 1991), and for launching powerful jets and winds through the magnetocentrifugal mechanism (Königl & Pudritz 2000; Shu et al. 2000). They are also the birthplace of planets.

Low-mass stars form in dense cores of molecular clouds. The cores are observed to rotate slowly (Goodman et al. 1993). It is generally expected that the conservation of angular momentum during the core collapse would automatically lead to the formation of a rotationally supported disk. The expectation is borne out by both semi-analytic calculations (e.g., Terebey, Shu, & Cassen 1984) and numerical simulations (e.g., Bodenheimer et al. 1990; for reviews of early work, see Bodenheimer 1995 and Boss 1998). However, the median value of the angular momenta measured for the cores (Goodman et al. 1993) is much higher than that inferred for circumstellar disks (Beckwith & Sargent 1993), by an order of magnitude or more (Bodenheimer 1995). Apparently, a considerable amount of angular momentum must be lost from the system in the process of core collapse and disk formation.

A well-known mechanism for angular momentum removal is magnetic braking. Magnetic fields are believed to play an important role in the formation of low-mass stars in relative isolation (Shu et al. 1987; McKee et al. 1993; Mouschovias & Ciolek 1999). Polarization maps of dust continuum emission have revealed ordered magnetic fields in many dense cores (see Girart, Rao, & Marrone 2006 for a spectacular example). The field strengths have been determined through Zeeman measurements in a number of them (Crutcher & Troland 2007). The importance of magnetic field is usually measured by the mass-to-flux ratio $\lambda$ in units of the critical value $(2\pi G^{1/2})^{-1}$. For L1544, arguably the best studied starless core (Tafalla et al. 1998; Crapsi et al. 2007), Crutcher & Troland (2000) inferred $\lambda \sim 8$ using the line-of-sight components of the field strength and column density. Correcting for projection effects may reduce $\lambda$ by a factor of 2 or more. In any case, there is ample observational evidence for both magnetic fields and rotation on the core scale. How the fields affect disk formation through magnetic braking of rotation is the focus of our investigation.

Previous studies of magnetic braking have mostly concentrated on the core formation phase of cloud evolution prior to the formation of a central object (Mouschovias & Paleologou 1979; Mestel & Paris 1979; Nakano 1989; Basu & Mouschovias 1994) or stopped shortly after a "seed" star has formed (Tomisaka 1998; Ziegler 2005; Banerjee & Pudritz 2006; Fromang, Hennebelle, & Teyssier 2006; Machida, Inutsuka, & Matsumoto 2007; see, how-

ever, recent work by Hennebell & Fromang 2007 and Hennebell & Teyssier 2007). What happens in the later, main protostellar mass accretion phase is less explored. Allen, Li, & Shu (2003, hereafter ALS03) followed numerically the protostellar collapse of moderately strongly magnetized cores (with the dimensionless mass-to-flux ratio $\lambda \leq 10$), and found that rotationally supported disks were not able to form in the ideal MHD limit. In hindsight, the suppression of disk formation is not too surprising, given that any disk that did form would be magnetically linked to a slowly rotating envelope of much larger moment of inertia and would lose its angular momentum quickly through magnetic braking. The braking is greatly enhanced by the equatorial pinching of field lines, which lengthens the magnetic lever arms (ALS03, Galli et al. 2006).

The catastrophic magnetic braking stood the traditional "angular momentum problem" of star formation on its head; the braking can be so efficient as to inhibit disk formation for a moderate level of cloud magnetization in the ideal MHD limit. The question is: under what condition will the rotationally supported disk reappear? To address this question, we go beyond ALS03 in two ways. First, we follow the collapse of magnetized, rotating dense cores using the spherical (as opposed to the cylindrical) version of the Zeus2D MHD code (Stone & Norman 1992a,b). The spherical geometry enables us to better resolve the angular distributions of the matter and magnetic field at small radii, where most of the magnetic braking is expected to occur. Second, we explore a wider range in the degree of cloud magnetization, $4 \leq \lambda \leq 400$. We find that the rotationally supported disk begins to be disrupted by magnetic braking for a dimensionless mass-to-flux ratio $\lambda \sim 100$, corresponding to an extremely weak field strength of order 1 $\mu$G for typical parameters of low-mass cores. An implication is that $\lambda = 1$ is not the only criterion for judging the dynamical importance of a magnetic field, as is often assumed. A relatively weak field of $1 \ll \lambda \lesssim 100$ can dominate the angular momentum evolution in the main accretion phase, because the field is amplified both by collapse and by rotation, and because the disk is braked over many rotation periods. Indeed, we find that even in the weakest field case that we have considered ($\lambda = 400$), the field is amplified enough for the magnetic pressure to dominate the thermal pressure in the disk and its surrounding region, at least in 2D. The ideal MHD calculations provide a limiting case for calibrating calculations that include nonideal effects, particularly ambipolar diffusion, that are currently underway (Mellon & Li, in preparation).

The rest of the paper is organized as follows. We describe the problem setup and the code used for computation in § 2. The numerical results are presented and discussed in § 3 through § 5. In § 6, we discuss the generic outcomes of the interplay between magnetic field and rotation during the protostellar mass accretion phase, including an extended region supported by a combination of toroidal magnetic field and rotation — a "magnetogyrosphere." Plausible observational evidence for such a structure in the Class 0 source IRAM 04191 is

discussed. The last section § 7 contains the main conclusions.

## 2. Model Formulation

### 2.1. Initial Condition

The early stage of low-mass star formation can be divided conceptually into two phases: a prestellar and a protostellar phase. The two are separated by a pivotal state (Li & Shu 1996), in which the central density formally goes to infinity. The pivotal state marks the end of core formation and the beginning of protostellar mass accretion. It is characterized by a large (formally infinite) density contrast between the center and the edge of the core. Idealizing the pivotal (t=0) state as a static singular isothermal sphere (SIS), Shu (1977) was able to obtain the well-known self-similar inside-out collapse solution for the protostellar phase of star formation. The present investigation is an extension of this work to those pivotal states that are both magnetized and rotating.

The self-similarity of the SIS is preserved in the presence of a dynamically important magnetic field, provided that the mass-to-flux ratio along each field line is constant. This condition, termed "isopedic" by Li & Shu (1996), is roughly satisfied in ambipolar diffusion-initiated formation of dense cores out of strongly magnetized clouds (Lizano & Shu 1989; Fiedler & Mouschovias 1993). In more weakly magnetized clouds, the nearly scale-free prestellar contraction of the isothermal gas right before the point mass formation would also drag the magnetic field of the dense core into a nearly isopedic configuration. ALS03 found a family of self-similar solutions for the isopedically magnetized, rotating, singular isothermal pivotal state, which turned out to be toroids. They have carried out an initial study of the collapse of the pivotal cores described by such solutions. Our investigation is a refinement and extension of theirs.

The singular isothermal toroids (SITs) are described, in a spherical polar coordinate system $(r,\ \theta,\ \varphi)$, by

$$\rho(r,\theta) = \frac{a^2}{2\pi G r^2} R(\theta), \tag{1}$$

$$\Phi(r,\theta) = \frac{4\pi a^2 r}{G^{1/2}} \phi(\theta), \tag{2}$$

$$V_\varphi(r,\theta) = a\ v(\theta), \tag{3}$$

where $a$ is the isothermal sound speed, which we take to be a constant, and the functions $R(\theta)$, $\phi(\theta)$ and $v(\theta)$ describe the angular distributions of the density $\rho$, magnetic flux $\Phi$, and rotation speed $V_\varphi$. We choose a fiducial value for the sound speed $a\ =\ 0.3$ km/s

(somewhat higher than 0.19 km/s, the sound speed of molecular gas at 10 K), to account for the (typically subsonic) nonthermal motions in dense cores (Myers 1995). The choice of $v(\theta)$ is discussed in depth in ALS03. Following their example, we set the rotation speed to a constant, i.e., $v(\theta) = v_0$. The density and magnetic flux distributions $R(\theta)$ and $\phi(\theta)$ are determined from a set of coupled ordinary differential equations (eqs. [14] through [17] of ALS03) and associated boundary conditions.

The toroid solutions are characterized by two free parameters, $v_0$ and $H_0$. The parameter $v_0$ specifies how fast the toroid rotates, while $H_0$ measures the amount of extra mass over the SIS that is supported by magnetic fields and rotation. For a given $v_0$, $H_0$ controls the magnetic field strength. ALS03 considered a number of combinations of $v_0$ and $H_0$, including $v_0 = 0, 0.125, 0.25$ and $0.5$ for $H_0 = 0.25$, and $H_0 = 0.125, 0.25$ and $0.5$ for $v_0 = 0.25$. They found no evidence for a rotationally supported disk in any of their simulations, which have dimensionless mass-to-flux ratios ranging from $\lambda = 2.77$ to 10. The result indicates that magnetic braking is very efficient, even for a magnetic field that is too weak to provide the bulk of support against self-gravity as a whole. On the other hand, a rotationally supported structure (a disk or a ring) is expected in the limit of zero magnetic field. As the field strength increases from zero, there must be a transition from a regime where a rotationally supported structure is formed to a regime where it is completely suppressed. Quantifying how this transition occurs is one of the main goals of the current investigation.

We will first focus on a specific combination of parameters, $v_0 = 0.5$ and $H_0 = 0.4$. For a fiducial isothermal sound speed $a = 0.3$ km/s, the choice $v_0 = 0.5$ corresponds to an angular speed 3 km s$^{-1}$ pc$^{-1}$ on the scale of 0.05 pc, the typical radius of a dense core (Myers 1995). The angular speed is within, although on the high side of, the range of velocity gradient inferred observationally by Goodman et al. (1993) for a collection of NH$_3$ cores (see their Fig. 1b). The relatively high rotation rate is chosen so that any rotationally support structure that may form is adequately resolved; slower rotations are expected to be braked more easily. For $v_0 = 0.5$, the choice $H_0 = 0.4$ yields a dimensionless mass-to-flux ratio along each field line $\lambda = 4$, consistent with the value inferred in the well-studied core L1544 (Crutcher & Troland 2000), after correcting for projection effects. It produces a distribution of (vertical) magnetic field on the equator

$$B_{\mathrm{eq}} = 24.5 \left( \frac{a}{0.3 \text{ km/s}} \right)^2 \left( \frac{0.05 \text{ pc}}{r} \right) (\mu G). \tag{4}$$

The rotating, magnetized singular isothermal toroid specified by $v_0 = 0.5$ and $H_0 = 0.4$ is shown in Fig. 1. Compared with the SIS of the same isothermal sound speed, the SIT has an enhanced density on the equator (by a factor of 2.25), due to extra support by the magnetic field and, to a lesser extent, rotation. The density is depleted in the polar region as

matter settles along the field lines, producing the toroid appearance. The magnetic pressure dominates the thermal pressure in the evacuated polar region, within a half opening angle of 40° of the axis. Outside the region (where most of matter resides), the thermal pressure dominates, with a plasma-$\beta = 7.68$ on the equator. This magnetic field, although too weak to prevent the core from collapsing inside out, is strong enough to suppress the formation of a rotationally supported disk completely, as we demonstrate below (see also ALS03). Indeed, even a much weaker magnetic field can modify the process of disk formation significantly in the ideal MHD limit.

To quantify the effects of field strength on magnetic braking and disk formation, we will reduce the field strength of the toroid shown in Fig. 1 by various constant factors everywhere, keeping the distributions of density and rotation speed fixed. We consider a wide range in the degree of magnetization, corresponding to $\lambda = 400, 200, 133, 80, 40, 20, 13.3, 8$, and 4 (see Table 1). For reference, $\lambda = 100$ corresponds to a field strength of merely 1 $\mu$G on the core scale of 0.05 pc (for the fiducial value of sound speed), well below the median field strength ($\sim 6\ \mu G$) in the cold neutral structures of HI gas (Heiles & Troland 2005). The field strength in dense cores of molecular clouds is unlikely to be as low as 1 $\mu$G, but we include cases with high values of $\lambda$ to illustrate the transition from disk formation to suppression. For more turbulent (perhaps massive star formation) regions where the effective sound speed is much higher than 0.3 km/s, even the very large $\lambda$ cases may become relevant, as we emphasize in the discussion section.

A potential drawback of reducing the field strength without changing the distributions of density and rotation speed correspondingly at $t = 0$ is that the initial configuration is out of force balance. The weakening of magnetic support will induce large-scale infall motions at times $t > 0$. Infall motions on the core scale are observed, however, in a number of dense cores, including L1544 (Tafalla et al. 1998), with speeds typically of order half the sound speed. Such a subsonic motion is present in our standard model to be discussed in depth in § 3. The reduction of field strength by a uniform factor everywhere at $t = 0$ has the added advantage that the core collapse at $t > 0$ remains self-similar, which provides a powerful check on the numerical solution. The same advantage is preserved when we reduce the fiducial rotation speed at $t = 0$ by a uniform factor everywhere. The effects of initial rotation speed are discussed separately from those of initial field strength in § 5.

## 2.2. Boundary Conditions

The protostellar phase of low-mass star formation in magnetized cores is challenging to simulate in the ideal MHD limit. Once a central point mass is formed, it will carry

Table 1.  Model Parameters

| Model | $\lambda$ | $v_0$ | $B_c^a$ $(\mu G)$ |
|-------|-----------|-------|-------------------|
| B0 | $\infty$ | 0.5 | 0.0 |
| B1 | 400 | 0.5 | 0.25 |
| B2 | 200 | 0.5 | 0.49 |
| B3 | 133 | 0.5 | 0.74 |
| B4 | 80 | 0.5 | 1.23 |
| B5 | 40 | 0.5 | 2.45 |
| B6 | 20 | 0.5 | 4.90 |
| B7$^b$ | 13.3 | 0.5 | 7.35 |
| B8 | 8 | 0.5 | 12.3 |
| B9 | 4 | 0.5 | 24.5 |
| R0 | 13.3 | 0.0 | 7.35 |
| R1 | 13.3 | 0.125 | 7.35 |
| R2 | 13.3 | 0.25 | 7.35 |

Note. — (a) Initial equatorial field strength (see equation [4]). (b) Model B7 is the standard model to be discussed in depth in § 3.

along with it a finite amount of magnetic flux. The trapped flux would formally produce a split magnetic monopole (Galli & Shu 1993; Li & Shu 1997), causing the field strength to increase rapidly with decreasing radius ($\propto r^{-2}$). The rapid increase of field strength makes the Courant condition associated with the Alfvén speed prohibitively small close to the origin, where the grid is necessarily very fine, especially in the $\theta$ direction of the adopted spherical polar coordinate system.

To alleviate the numerical problem associated with the formation of a split magnetic monopole, we put the inner boundary of our computation domain at a fixed radius, $r_i = 10^{14}$ cm, or 6.7 AU. We are unable to follow the evolution of the flow inside $r_i$. However, for our adopted initial conditions, only a small fraction of the core mass has a low enough specific angular momentum to fall through the inner surface (or " inner hole") without magnetic braking; for the majority of the mass, extensive braking must occur in the computation domain to bring it to the inner surface. On this surface, we impose the standard "outflow" boundary conditions for the hydrodynamic quantities, i.e., the density, energy and tangential (to the surface) velocity components are copied from the first active zones into the ghost zones along the radial direction. The radial velocities in the ghost zones are set to the lesser of the radial velocity in the first active zone and zero. These conditions are a standard feature already implemented in the Zeus2D code (Stone & Norman 1992a,b) that is employed for our simulations.

The inner boundary conditions for the magnetic field require special attention. Since the poloidal components of the magnetic field are evolved through the method of constrained transport (Evans & Hawley 1988) in Zeus2D, their boundary conditions are imposed on the electromotive force (EMF) $\epsilon = \mathbf{V} \times \mathbf{B}$. We apply the standard Zeus2D "outflow" boundary conditions on the EMF to evolve the poloidal magnetic field. They produce a poloidal field that varies smoothly across the inner surface. The toroidal component of the magnetic field $B_\varphi$ is not evolved through the method of constrained transport, and it is possible to impose boundary conditions on $B_\varphi$ directly. We pick the simplest possible condition for the toroidal field in the ghost zones: $B_\varphi = 0$. It is in effect a torque-free boundary condition. The choice is motivated in part by the realization that, by the time a piece of core material reaches the (small) inner surface, most of its angular momentum would have been stripped away already. The remaining angular momentum would be too little to significantly twist the strong (split-monopole) field lines that thread the inner surface (see Galli et al. 2006, for a related discussion). Other prescriptions are possible. For example, Stone & Pringle (2001) enforced the negative stress condition $B_r B_\varphi \leq 0$, whereas Hawley & Krolik (2001) set the transverse components of the magnetic field to zero in their simulations of black hole accretion in a cylindrical coordinate system. We have experimented with other prescriptions for $B_\varphi$ in the ghost zones, including copying values from the first active zones, which produced a

somewhat stronger outflow along the axis compared with the torque-free case. The outflow is weak by the standard of the powerful jets and winds observed in young stars (ALS03), and will be easily masked by them. In any case, the simple torque-free boundary condition does not directly affect the braking of the bulk of the core material that accretes through the equatorial region (including any disk that may form), the main focus of our investigation.

Boundary conditions are also required at the outer boundary. We set the outer radius of the computation domain to $r_o = 2 \times 10^{17}$ cm, slightly larger than the fiducial core radius of 0.05 pc. Within this radius, there is 3.8 $M_\odot$ of material for the initial density distribution shown in Fig. 1 (for $a = 0.3$ km/s), more than enough to form a typical low-mass star of 0.5 $M_\odot$. On the outer boundary, we impose the standard Zeus2D "outflow" boundary conditions for all quantities, including $B_\varphi$.

We assume that the core collapse remains symmetric with respect to the polar axis and the equatorial plane at all times. We adopt the standard Zeus2D boundary conditions for the axis. To enforce the equatorial boundary conditions, we mirror all quantities (including the three components of the magnetic field) in the upper quadrant to the lower quadrant at the beginning of each time step, and evolve the governing equations in both quadrants. This implementation of equatorial boundary conditions, although somewhat more expensive than the one already in Zeus2D, guarantees that the symmetry is enforced exactly. Spontaneous symmetry breaking is observed in MHD simulations of black hole accretion (Hawley & Krolik 2001; Stone & Pringle 2001). We will relax the equatorial symmetry in future 3D simulations.

## 2.3.  Code Modification and Problem Setup

For our axisymmetric problem, we use the Zeus2D MHD code of Stone & Norman (1992a,b) in spherical polar coordinate system. The code is well suited for our investigation of magnetic braking, since the propagation of (torsional) Alfvén waves is treated accurately with the method of characteristics. The main modification that we made to the code is to improve the method for obtaining the values of gravitational potential at the inner and outer boundaries; they are needed for solving the Poisson equation for the self-gravity of the material inside the computational domain. The method of multipole expansion in Zeus2D performs poorly when mass is near a boundary and requires a large number of terms to accurately determine the gravitational potential. Instead, we transform Green's function from the multipole solution to an elliptic integral solution (Cohl & Tohline 1999). We can then directly sum up the contributions of the masses in all active cells to the gravitational potential at a given location on the boundary, as in Fromang et al. (2004). We also modified the equation of state to change smoothly from isothermal to adiabatic around a critical

density of $10^{-13}$ gm cm$^{-3}$, to mimic the effects of radiation trapping at high densities.

To ensure good resolution on both large and small scales, a logarithmically spaced grid is used in the radial direction. We divide the computational domain between the inner ($r_i = 10^{14}$ cm) and outer radius ($r_o = 2 \times 10^{17}$ cm) into 120 shells, each having a width that is 6% larger than that of the shell interior to it. Since both $\Delta r$ and $r\Delta\theta$ vary linearly with the radius, the grid does not contain cells of large aspect ratios often seen in logarithmic grids in cylindrical coordinate system. The width of the first shell is $1.10 \times 10^{13}$ cm, much smaller than the inner radius $r_i$. In the polar direction, we divide the region between the upper ($\theta = 0$) and lower axis ($\theta = \pi$) into 119 uniform wedges, each with an opening angle of $1.5°$. As mentioned earlier, half of the grid (between $\theta = \pi/2$ and $\pi$) is used for enforcing mirror symmetry across the equator.

We begin the collapse calculation with a static, dense core. To initiate the collapse, we add a point mass of $M_0 = 3a^3r_i/G$ (where $a$ is the isothermal sound speed and $r_i$ the radius of the inner hole) at $t = 0$. This mass is 1.5 times the mass enclosed within $r_i$ for a SIS of sound speed $a$, and slightly larger than that enclosed within the same radius for the magnetized SIT shown in Fig. 1 ($2.8a^3r_i/G$). As the collapse proceeds, the density is depleted preferentially in the polar region, where the magnetic field is strong and matter slides more or less freely along the field lines to the center (ALS03). To prevent the Alfvén time step from dropping to prohibitively small values, we adopt a density floor of $10^{-19}$ gm cm$^{-3}$ on the inner half of the (logarithmic) radial grid (within $5.3 \times 10^{15}$ cm). The occasional use of density floor in the polar region is expected to have little dynamical effect, since the dynamics there are controlled by the magnetic field. We have experimented with different choices of the floor value and confirmed the expectation.

## 3. Standard Model

The rotating, magnetized core that we adopt as the initial configuration for the collapse calculation is specified by two parameters: the dimensionless mass-to-flux ratio $\lambda$ and the rotation speed $v_0$ in units of the sound speed. We will explore a wide range of values for $\lambda$ in § 4 and several values for $v_0$ in § 5. In this section, we focus on a model with a particular combination of parameters $\lambda = 13.3$ and $v_0 = 0.5$ (Model B7 in Table 1); it serves as the standard against which others models are compared. The choice $\lambda = 13.3$ corresponds to a moderate field strength of 7.35 $\mu$G on the scale of the typical core radius 0.05 pc (not much higher than the median field strength of $\sim 6.0$ $\mu$G inferred by Heiles & Troland (2005) for the cold neutral HI structures), and $v_0 = 0.5$ is chosen to ensure that any rotationally supported structure that may form is large enough to be adequately resolved. More importantly, it

turns out that the combination yields a collapse solution that is roughly self-similar in time, as expected from the self-similar initial configuration adopted. The self-similarity gives us confidence on the numerically obtained solution.

### 3.1.   Collapse Solution at a Representative Time

Fig. 2 shows a snapshot of the standard model at a representative time $t = 6.4 \times 10^{11}$ sec (or $\sim 2 \times 10^4$ yrs after the initiation of collapse), comparable to the typical ages estimated for Class 0 sources. The snapshots at other times are largely similar (to be quantified below), which motivates us to introduce a set of dimensionless variables:

$$\alpha = 4\pi G t^2 \rho(r, \theta, t), \ \mathbf{b} = \frac{G^{1/2}t}{a}\mathbf{B}(r, \theta, t), \ \mathbf{v} = \frac{\mathbf{V}(r, \theta, t)}{a}, \ x = \frac{r}{at}. \tag{5}$$

If the collapse is strictly self-similar, the dimensionless density $\alpha$, magnetic field $\mathbf{b}$ and velocity $\mathbf{v}$ would be functions of the dimensionless self-similar radius $x = r/(at)$ and polar angle $\theta$ only, and the solution would look identical at different times except for a scaling factor. Equation (5) can be used to obtain the dimensional units for any dimensionless quantity to be used below, particularly in figures; the plotted quantities will be dimensionless unless noted otherwise explicitly.

Broadly speaking, there are four dynamically distinct regions. At large (cylindrical) distances, the core material collapses inward, dragging along magnetic field lines, particularly in the equatorial region. We term this region the "collapsing envelope" or "Region I." Most of the collapsing material from the envelope is channeled into the equatorial region, forming a flattened "pseudodisk" or "Region II." The pseudodisk is squeezed from above by an expanding "magnetic bubble" (or "Region III") that lies at intermediate latitudes. The pseudodisk supports the bubble from below. On the other side of the bubble, closer to the polar axis, lies "Region IV," where matter slides down well-ordered field lines, forming a low-density "polar funnel." We consider the outflowing region near the axis part of "Region III;" it is a continuation of the bubble to large distances.

The boundaries between the various regions show up most clearly in the map of the magnetic twist, defined as the ratio of the toroidal to poloidal field strength $B_\varphi/|B_p|$ (see Fig. 3). To be specific, we define the region dominated by the (negative) toroidal magnetic field (i.e., $-B_\varphi > |B_p|$) as the bubble ("Region III"). It is surrounded by the polar funnel to the left, the collapsing envelope to the right, and the pseudodisk from below. The collapsing envelope is separated from the bubble by a "magnetic wall," produced by the deceleration of the magnetized collapsing envelope against the bubble; the deceleration leads to a pileup of the field lines. The decelerated material slides along the compressed field lines nearly

vertically towards the equator. Before hitting the equator, the downward moving material is deflected towards the origin by a strong (thermal) pressure gradient to join the pseudodisk beneath the magnetic bubble.

The equatorial part of the collapsing envelope joins onto the pseudodisk more directly. It slows down near the outer edge of the pseudodisk before being reaccelerated towards the center by gravity. The deceleration and reacceleration show up more clearly in Fig. 4, where we plot the radial component of the velocity on the equator as a function of radius. The curve of radial speed has a peak around $x_\mathrm{s} \approx 0.5$, where $v_r$ is close to zero; indeed, the gas there is actually slowly expanding rather than collapsing. We identify the region near the stagnation radius $x_\mathrm{s}$ as a "magnetic barrier", as opposed to a "centrifugal barrier." The reason is that, at this location, the rotation speed is well below that needed for the centrifugal force to balance the gravity (see Fig. 4, where both speeds are plotted). There is tantalizing evidence for such a structure in the Class 0 source IRAM 04191, as we discuss in § 6.2. It bounds the pseudodisk from outside. Note that the infall speeds at large distances are close to half the sound speed, comparable to that inferred observationally in the dense core L1544 (as mentioned earlier) and in the envelope of IRAM 04191 (Belloche et al. 2002), except near the outer boundary, where the edge effect becomes significant. The large-scale infall is induced by the reduction of the full field strength at $t = 0$ (from $\lambda = 4$ to 13.3), which weakens the initial magnetic support relative to self-gravity.

After passing through the stagnation region at the magnetic barrier, the pseudodisk material on the equator collapses quickly inward. The rapid infall leads to a spinup of the collapsing material, as shown in Fig. 4. The inward increase in rotation speed is slowed down around a dimensionless radius $x_\mathrm{c1} \sim 0.1$, and levels off near $x_\mathrm{c2} \sim 0.05$. A glance at Fig. 3 shows that this is the region where the magnetic bubble is initiated. In this region, the radial infall is temporarily slowed down, as a result of increased centrifugal support; in other words, a centrifugal barrier is encountered. The slowdown of infall allows more time for the magnetic braking to operate. Interior to $x_\mathrm{c2}$ is a strongly magnetized region dominated by the central split monopole. Here, the rotation speed drops steadily with decreasing radius, as a result of efficient braking by the strong magnetic field. The loss of centrifugal support causes the equatorial material to resume its rapid collapse towards the center. The rapid infall and slow rotation leave no doubt that a rotationally supported disk is not produced in this standard model. In particular, the rotation speed at small radii is well below that needed to provide centrifugal support against gravity (compare the top two curves in Fig. 4). Upon arriving at the inner hole, the infall material has lost most of its original angular momentum along the way. The questions is: how does the stripping of angular momentum occur mechanically?

The key to answering the above question lies in the magnetic bubble (Region III). It

is powered by the pseudodisk (Region II). The material in the pseudodisk spins up as it collapses, producing a growing toroidal magnetic field, which in turn leads to a buildup of magnetic pressure. The over-pressure in the region is relieved by expansion along the path of least resistance. Expansion is restricted to the left of the region or vertically up by the strong monopole field. It cannot freely expand horizontally outward either; it is contained by the ram pressure of the infalling material. These constraints force the over-pressured region to expand outward at an acute angle with respect to the equatorial plane, producing a bubble where the bulk of the angular momentum stripped from the collapsing pseudodisk is stored.

## 3.2. Approximate Self-Similarity in Time Evolution

Self-similarity not only provides a check on the numerically obtained solution, but also enables us to discuss the solution in a time-independent way. A good indicator of the self-similarity of the collapse solution is the evolution of the central point mass $M_0$. In a strictly self-similar solution (such as Shu's inside-out collapse solution), the mass should increase linearly with time. The change of $M_0$ with time for the standard model is shown in Fig. 5. Overall, there is a nearly linear increase of the point mass with time, except near the origin. The initial deviation is caused by the finite size of the inner hole (which breaks the self-similarity of the initial configuration), and the point mass that was put at the center at $t = 0$ to induce collapse. After a short period of initial adjustment (of order $10^{11}$ sec), the mass-time curve becomes remarkably straight, although there are low-amplitude oscillations. As we discuss in detail in § 4.2, the oscillation is caused by magnetic flux accumulation near the center, which produces a split magnetic monopole that reconnects episodically across the equatorial plane. The reconnection events make it impossible for the collapse to settle into a strictly steady state in the self-similar space. Their influence on the collapse solution increases with the strength of the magnetic field. For the standard model, the field is still weak enough that the self-similarity is preserved approximately.

To demonstrate the approximate self-similarity more vigorously, we use a closure relation that any self-similar collapse solution must satisfy. The relation is derived from the equation of mass conservation

$$\frac{\partial M(r,t)}{\partial t} = -2\pi \int_0^\pi \rho r^2 \sin(\theta) V_r d\theta, \tag{6}$$

where $M(r,t)$ is the mass enclosed within a radius of $r$ at the instant of time $t$. It is given by

$$M(r,t) = M_0(t) + 2\pi \int_0^r \int_0^\pi \rho \tilde{r}^2 \sin(\theta) d\theta d\tilde{r}, \tag{7}$$

where $M_0$ is the point mass at the center. In terms of the dimensionless self-similar variables introduced in equation (5), the mass $M(r,t)$ can be written into

$$M(r,t) = \frac{a^3 t}{2G} m(x), \tag{8}$$

where

$$m(x) = m_0 + \int_0^x \int_0^\pi \alpha(\tilde{x}, \theta)\tilde{x}^2 \sin(\theta)d\theta d\tilde{x}, \tag{9}$$

is the dimensionless mass enclosed within a dimensionless radius $x$, and $m_0$ is the dimensionless point mass at the center. Using equation (8), we can express the left-hand side of equation (6) as

$$\frac{\partial M(r,t)}{\partial t} = \frac{a^3}{2G}\left[m(x) - xm'(x)\right], \tag{10}$$

where $m' = dm/dx = \int_0^\pi \alpha(x,\theta)x^2 \sin(\theta)d\theta$ from equation (9). Equating the right-hand side of equation (10) with the right-hand side of equation (6) yields

$$m(x) = \int_0^\pi \alpha(x,\theta)x^3 \sin(\theta)d\theta + \int_0^\pi \alpha(x,\theta)x^2 \sin(\theta)(-v_r)d\theta = \int_0^\pi \alpha(x,\theta)x^2 \sin(\theta)(x - v_r)d\theta, \tag{11}$$

which is the equation of mass conservation in the self-similar space. It has a simple physical meaning. The term on the left-hand side is the dimensionless mass enclosed within a sphere of radius $r = xat$ that expands linearly in time (for a fixed $x$). This mass can be increased due to either the expanding volume (which is proportional to the first term on the right-hand side of the first equality) or advection of material into the sphere from outside (proportional to the second term). Note that the combination $x - v_r$ on the right hand side of the second equality is simply the speed with which the sphere is expanding relative to the material that moves at a radial speed of $v_r$.

The dimensionless mass distribution $m(x)$ can be evaluated in another way, using equations (9), which states that the mass inside a given radius is simply the sum of all mass (including the point mass) up to that radius. In a strictly self-similar solution, the masses determined independently from equations (9) and (11) should coincide. In our standard model, we find that the mass distribution $m(x)$ from equation (9) remains more or less steady in time everywhere, whereas that from equation (11) shows large variations from one time to another inside a dimensionless radius of $\sim 0.3$. The variations are caused by unsteady mass accretion due to frequent reconnection events. The variations are much reduced if we average the mass distributions over timescales that are long compared with the durations of individual reconnection events but short compared with the total simulation time, which is $\sim 1.6 \times 10^{12}$ sec. The result is illustrated in Fig. 6, for a representative period of time between $t = 3.0 \times 10^{11}$ and $7.5 \times 10^{11}$ sec; the averaging is done over 90 outputs taken at intervals

of $5 \times 10^9$ sec. Except for some wiggles within a small radius of $\sim 0.1$, the two independently determined average mass distributions agree rather well. The maximum discrepancy (of order $\sim 4\%$) occurs around $x \sim 0.5$, close to the outer edge of the pseudodisk. Perfect agreement is not to be expected, given the finite sizes of the inner and outer boundaries of the computation domain. The good agreement suggests that the collapse solution fluctuates around a well defined self-similar solution, with a mass distribution close to those shown in the figure.

A similar closure relation can be derived for the angular momentum, allowing further verification of the approximate self similarity of this solution. We start from the equation for angular momentum conservation:

$$\frac{\partial L(r,t)}{\partial t} = -\int \rho \varpi V_\varphi V_r dS + \frac{1}{4\pi} \int B_\varphi B_r \varpi dS, \tag{12}$$

where $L(r,t)$ is the angular momentum enclosed within a sphere of radius $r$ at a time $t$, and the two terms on the right hand side are, respectively, the angular momentum advected into the sphere by fluid motion per unit time and the magnetic torque acting on the surface of the sphere, $S$. The quantity $\varpi$ is the cylindrical radius. If the collapse is strictly self-similar, the angular momentum can be written as

$$L(r,t) = \frac{a^5 t^2}{2G} l(x), \tag{13}$$

where the dimensionless angular momentum $l(x)$ is given by

$$l(x) = \int_0^x \int_0^\pi \alpha v_\varphi \tilde{x}^3 \sin^2(\theta) d\theta d\tilde{x}. \tag{14}$$

Using equation (13), we can express the left-hand side of equation (12) as

$$\frac{\partial L(r,t)}{\partial t} = \frac{a^5 t}{2G} \left[ 2l(x) - xl'(x) \right], \tag{15}$$

where $l' = dl/dx$. Equating the right-hand side of equation (15) with the right-hand side of equation (12) yields

$$l(x) = \frac{1}{2} \left[ \int_0^\pi \alpha(x,\theta) v_\varphi x^4 \sin^2(\theta) d\theta + \int_0^\pi \alpha(x,\theta) v_\varphi x^3 \sin^2(\theta)(-v_r) d\theta + \int_0^\pi b_r b_\varphi x^3 \sin^2(\theta) d\theta \right] \tag{16}$$

which is the equation of angular momentum conservation in the self-similar space. Compared with the dimensionless equation for mass conservation (eq. [11]), there is an extra factor of 1/2 on the right hand side (resulting from the quadratic rather than linear dependence of

angular momentum on time) and an additional (third) term inside the square bracket that comes from magnetic braking. The first two terms have the usual interpretation: they are, respectively, the increase of angular momentum inside a sphere of constant dimensionless radius $x$ due to the expansion of the sphere and matter moving across the surface.

We plot in Fig. 7 the averaged distributions of angular momentum computed from equations (14) and (16), over the same 90 outputs used for Fig. 6. The two distributions agree remarkably well, again indicating that the solution is nearly self-similar.

### 3.3. Mass and Angular Momentum Distribution in Self Similar Space

It is instructive to examine the dimensionless mass distribution $m(x)$ more closely. In Fig. 6, we plotted the two terms on the right hand side of equation (11) separately. The contribution to $m(x)$ due to the advection term (proportional to the infall speed $-v_r$) has a minimum value of $\sim 0.5$ near the radius $x \sim 0.5$, where the infall is slowed down at the magnetic barrier. It increases inwards as the temporarily slowed down material picks up infall speed (see Fig. 4). The dip is compensated, to a large extent, by a peak in the contribution due to volume expansion (for a sphere of fixed dimensionless radius $x$). The peak is a result of the density enhancement in the low-$v_r$, stagnation region.

Note that the dimensionless mass $m(x)$ approaches a finite value as $x \to 0$. The mass near the origin is simply the central point mass. It has a dimensionless value of $m_0 = 2GM_0/(a^3t) \sim 3.6$. This mass is nearly twice the classical value for the inside-out collapse of a singular isothermal sphere (SIS), which has $m_0 = 1.95$ in our mass units (Shu 1977). Part of the increase comes from the fact that the initial configuration for collapse is, on average, denser than the SIS. Another reason is that, unlike the SIS, the initial configuration is out of exact force balance, which induces a subsonic, global contraction. The mass accretion onto the point mass is hindered, on the other hand, by rotation, which tends to slow down the collapsing material through centrifugal force. Indeed, in the absence of a magnetic field, most of the collapsed material in the standard model would be rotationally supported rather than falling to the center. The relatively high rate of *central* mass accretion is made possible by continuous magnetic braking.

To understand the effects of magnetic braking on the angular momentum evolution in more detail, we plot in Fig. 7 the individual terms on the right hand side of eq. (16). As with the mass distribution $m(x)$, the contribution to the angular momentum $l(x)$ inside a sphere of radius $x$ due to advection (second term) shows a dip near $x \sim 0.5$, as a result of infall deceleration, whereas that due to volume expansion (first term) shows a peak in the

same region, as a result of angular momentum pileup. A crucial difference is that, unlike $m(x)$, $l(x)$ does not asymptote to a finite value near the origin. Rather, it approaches zero at small radii. The implication is that, *although mass falls onto the central object at a relatively high rate, little angular momentum is accreted.* The angular momentum removal can be seen most clearly by comparing the angular momentum advected into a sphere by mass motion (second term) and that removed by magnetic braking from the same surface (third term). ¿From Fig. 7, we find that these two terms nearly cancel each other over an extended region (up to $x \sim 0.4$). The near cancellation points to a detailed balance of inward and outward transport of angular momentum, which enables a large amount of matter to be accreted, but little angular momentum. The balance is at the heart of the magnetic braking-driven mass accretion.

## 3.4. Magnetic Bubble

The magnetic bubble plays a key role in the angular momentum redistribution. Angular momentum is transported outward in this region through both outflowing gas and magnetic torque. In the standard model, roughly half of the angular momentum advected across a given radius by the equatorial, infalling, pseudodisk is carried away by the outflowing material; the other half by the highly twisted magnetic field. It is the toroidal field that drives the expansion of the bubble, as in the so-called "magnetic tower" investigated by Lynden-Bell (2003). The strength of the toroidal field is determined by the ambient pressure that confines the bubble in the lateral direction. In Fig. 8, we plot the total pressure and its various components as a function of angle at a representative radius $x = 0.3$ (roughly the middle radius of the bubble). The total pressure does not vary much at different angles, but it is dominated by different components in different regions. In the pseudodisk near the equator ($\theta = \pi/2$), it is dominated by the thermal pressure, because of high density. The pressure due to the toroidal magnetic field dominates at intermediate latitudes inside the bubble. It is more than an order of magnitude stronger than the pressure due to the poloidal field, and a factor of $\sim 2.5$ times larger than the thermal pressure. The bubble is therefore magnetically dominated, with a plasma-$\beta$ less than unity. The polar region is even more strongly dominated by the magnetic field, although by the poloidal rather than the toroidal component.

The kinematics of the three regions are also quite distinct. Over most of the equatorial pseudodisk, the infall and rotation speeds are comparable. Both are supersonic and super Alfvénic. The infall dominates the rotation in the polar funnel. It is supersonic but sub-Alfvénic (because of a high Alfvén speed associated with the strong poloidal field and low

density). The bubble, on the other hand, is a toroidally dominated structure in both magnetic field (by definition) and velocity field. The mass-weighted average rotation speed inside the bulk of the bubble (within a dimensionless radius $x = 1$) is about $2.2\, a$, whereas that for the average poloidal speed is slightly less than the sound speed $a$, which is smaller than the Alfvén speed. The meridian flow inside the bubble is thus generally sub-Alfvénic. It is in contact, through magnetosonic waves, with the base of the bubble, where a toroidal magnetic flux is constantly generated out of the poloidal flux (dragged in from large distances) by differential rotation. It is the continuous insertion of new toroidal flux into the bubble that drives it to expand (Lynden-Bell 2003).

The sub-Alfvènic motions indicate that the bubble can be viewed as being more or less quasi-static in the meridian plane. It is then natural to ask: what supports the bubble against the gravity (which comes mostly from the point mass at the radii of the bubble, with some contribution from the self-gravity)? It turns out that the support is provided mainly by the rotation and toroidal magnetic field; the latter acts on the bubble material through a combination of magnetic pressure gradient and tension force. In some sense, the slowly expanding bubble is a partly rotationally and partly magnetically supported structure that forms in place of the purely rotationally supported structure that would form in the absence of magnetic braking. It is a generic, potentially observable structure that we will discuss in some depth in § 6.2.

The bubble is a depository of mass and angular momentum. The dimensionless mass and angular momentum are more or less constant in time, with small fluctuations due to reconnection events. The bubble has an average mass $m_b \sim 2.3$ within a radius of $x = 1$, which is about 64% of the central point mass ($m_0 \sim 3.6$). It carries a total dimensionless angular momentum of $\sim 1.4$. The average specific angular momentum is therefore $l_b \sim 0.61$. It corresponds to a centrifugal radius of

$$x_c \sim \frac{2l_b^2}{m_0} \sim 0.2. \tag{17}$$

If a fraction of the rotating bubble material were to recollapse at a time $t$ in the absence of further magnetic braking, it would form a disk of size comparable to the centrifugal radius

$$r_c \sim 10^3 \left( \frac{a}{0.3\text{km/s}} \right) \left( \frac{t}{10^5\text{yr}} \right) \text{ AU} \tag{18}$$

around the central object. We will discuss the possibility of late-time disk formation in § 6.2.

Another way to gauge the dynamic state of the bubble is to consider its energies. The total (thermal, kinetic and magnetic) energy is close to the gravitational binding energy in the potential of the central point mass. It is well below the gravitational binding energy when

the self-gravity of the core is also taken into account. The bulk of the bubble material cannot escape to infinity by itself. It is expanding slowly outward only because it is being pushed continuously from below, as more and more mass and toroidal magnetic flux being inserted into the bubble. If for some reason the insertion were to stop suddenly, the bubble (at least a portion of it) may recollapse to form a disk. The existence of a large amount of bound (bubble) material of high specific angular momentum not far from the center indicates that, *although magnetic braking can allow mass to fall into the center at a high rate, the overall angular momentum problem is not decisively resolved.* We will speculate in the discussion section implications of this situation, including the possible role of protostellar winds in dispersing away the bubble and the angular momentum accumulated in it.

## 4.    Effects of Magnetic Field Strength

Having examined in some detail a standard model with a specific mass-to-flux ratio of $\lambda = 13.3$, we now turn our attention to cases with different degrees of magnetization. We will first concentrate on the relative weak field cases with $\lambda$ between 400 and 13.3 (§ 4.1). The strong field cases with $\lambda = 4$ and 8 behave quite differently; they will be discussed separately in § 4.2.

### 4.1.    Relatively Weak Field Cases

Before going into details of the various collapse solutions, we first discuss their general behaviors based on the dimensionless central mass $m_0$. It is defined as $m_0 = 2GM_0/(a^3t)$, where $M_0$ is the central mass. The dimensionless mass $m_0(t)$ at any given time is simply the averaged mass accretion rate up to that time, normalized by $a^3/(2G)$. It is plotted as a function of time in Fig. 9 for all cases with $\lambda$ between 13.3 and 400. Since mass accretion is driven by magnetic braking, which in turn depends on the field strength, one expects $m_0$ to decrease as $\lambda$ increases. This trend is indeed seen in Fig. 9, except for the three most weakly magnetized cases ($\lambda = 400$, 200 and 133). For these extremely weak field cases, the trend is not as clear, especially at late times. It turns out that these are the cases where a rotationally-supported, equilibrium disk is present. They are discussed in § 4.1.1. Even the weakest field case has a significant mass accretion, however, at a rate well above that in the non-magnetic case ($\lambda = \infty$; the lowest curve in the figure) at late times. The initial burst of mass accretion in the non-magnetic case comes from the finite size of the inner hole and the presence of a small "seed" mass that was placed at the center to induce collapse, rather than any angular momentum redistribution.

The initial burst in mass accretion is also present in the magnetized cases, although it is relatively inconspicuous in the two strongest field cases ($\lambda = 13.3$ and 20). In both cases, the (average) mass accretion rate quickly approaches a plateau, indicating that a nearly self-similar state is reached; the small oscillations are related to magnetic flux accumulation in the central hole (see § 4.2 below). Indeed, the collapse solution in the $\lambda = 20$ case is very similar to that of the standard $\lambda = 13.3$ case discussed in the last section. It will not be discussed separately further.

The intermediate cases with $\lambda = 40$ and 80 are particularly interesting. They represent the transition from the weaker field cases where a rotationally-supported, equilibrium disk is present to those where the disk formation is suppressed. These cases are discussed in § 4.1.2.

### 4.1.1. Disk Formation in Extremely Weak Field Cases

The rotating collapse is modified significantly by the magnetic field in the case of $\lambda = 400$, which corresponds to a field strength of merely 0.25 $\mu G$ at the typical core radius of 0.05 pc. In the absence of any magnetic field, the initial configuration collapses into a self-gravitating ring (centered at a dimensionless radius $x = 0.05$). The ring formation is suppressed by the weak field, and a disk is produced in its place, as shown in Fig. 10. The figure is a snapshot at a representative time $t = 2.0 \times 10^{12}$ sec, plotted in self-similar quantities. The snapshots at other times are similar to the one shown. Prominent in the figure is a flatten high-density disk, surrounded by a lower density, more puffed up "corona." Despite the weakness of the initial field, the magnetic pressure due to toroidal field actually dominates the thermal pressure, by a factor of $\sim 2.5$ on average. The inner part of the disk is more strongly magnetized, with the ratio of magnetic to thermal pressures greater than 10 inside a radius of $\sim 0.01$, perhaps as a result of a shorter orbital period, which allows the field lines to wind up more turns in a given time. The poloidal magnetic field inside the disk is, on the other hand, very weak, with an energy of order 0.1% of the thermal energy on average. The weak poloidal field is susceptible to magnetorotational instability (MRI; Balbus & Hawley 1998). The role of MRI, as opposed to simple twisting of a pre-existing poloidal field, in redistributing angular momentum in the disk remains to be quantified (see discussion in § 6.3 below).

The disk is rotationally supported. The best evidence for rotational support comes from Fig. 11, where the rotation speed of the material on the equator is compared to the equilibrium rotation speed computed from the (total) gravitational potential at the representative time shown in Fig. 10. Inside the disk (within a radius of about 0.1), the actual rotation speed is close to, but slightly less than, the equilibrium value. The small deviation is caused

by additional supports from thermal pressure and magnetic forces. Outside the disk, the rotation speed is substantially less than the equilibrium value. Also plotted in Fig. 11 is the radial component of the velocity of the material on the equator. It shows an outer region that infalls supersonically, and an inner region that is nearly static. The former is expected of the collapsing envelope, whereas the latter is consistent with a rotationally-supported disk that is close to an equilibrium in the radial direction. The disk does have a small, non-zero, radial velocity, which is responsible for transporting material from the outer disk to the inner disk. The transport, driven by angular momentum redistribution, enables mass accretion onto the central object, at a dimensionless rate $\sim 0.7$, which is about 1/3 of the rate for SIS (Shu 1977).

The rate of mass accretion from the disk to the central object is small compared to that from the envelope to the disk. As a result, the bulk of the material collapsed from the envelope is stored in the disk rather than the central object. The relative smallness of the central mass is also evident from the equilibrium rotation curve shown in Fig. 11, which deviates significantly from a Keplerian curve, especially in the outer part of the disk. The deviation, particularly the bump near the disk edge around $x \sim 0.1$, is an indication that self-gravity is important; indeed, it dominates the gravity of the central mass beyond a dimensionless radius $\sim 0.04$.

The $\lambda = 200$ and 133 cases are qualitatively similar to the $\lambda = 400$ case. They all produce a persistent, rotationally supported disk. There are some quantitative differences, however. The magnetic barrier, barely noticeable in the weakest field case, are rather prominent in the stronger field cases. Also, as the field strength increases, the disk becomes more dynamically active in the radial direction. The infall speed can occasionally become supersonic in some (usually narrow) regions, indicating that sporadic disk disruption has begun already in localized places, especially in the $\lambda = 133$ case. The disruption becomes more widespread and persistent as the field strength increases further.

### 4.1.2. Transition from Disk Formation to Suppression

Sustained disk disruption happens in the case of $\lambda = 80$. The disruption is illustrated in Fig. 12, where the radial component of the velocity, $v_r$, on the equator is plotted at a representative time $t = 2 \times 10^{12}$ sec. Unlike the weaker magnetic field case of $\lambda = 400$ shown in Fig. 11, where the radial velocity nearly vanishes everywhere in the disk, $v_r$ is close to zero in four discrete (narrow) regions, with rapid, transonic or even supersonic, infall in between.

The stagnation point at the largest radius is the magnetic barrier, as in the standard,

stronger field case (see Fig. 4). In the standard case, there is a second stagnation point interior to the magnetic barrier, which we have interpreted as the centrifugal barrier, where the infall is slowed down temporarily and the magnetic braking is locally enhanced. In the $\lambda = 80$ case, the stagnation points interior to the magnetic barrier are also centrifugal barriers. The reason for the existence of more than one barriers can be seen from the upper curve in Fig. 12, where the specific angular momentum is plotted as a function of radius. Even though a good fraction (about half) of the angular momentum is removed at the first centrifugal barrier, there is still a significant amount left interior to it. The material recollapses quickly towards the center, spinning up at the same time, until a second centrifugal barrier is encountered. The slowdown allows more time for the fluid rotation to twist up the field lines. The magnetic braking removes enough angular momentum from the material in the equatorial region to enable it to recollapse for a third time, all the way to near the inner boundary, where the infall is rearrested by rotation. In some sense, the rotating material tries to settle into a rotationally supported disk, but the attempt is repeatedly frustrated by magnetic braking. The result is a collection of discrete rings that are temporarily supported by the centrifugal force, separated by regions of rapid collapse, where the rotational support is insufficient to balance the gravity. Note that in 3D, the rings may break up into arcs or clumps, some of which may become self-gravitating and form (sub-)stellar objects.

The material in the stagnation region near a centrifugal barrier loses a large fraction of its angular momentum, and collapses quickly inwards after exiting the region. Why is it possible to remove a large fraction of the angular momentum before the material begins collapsing dynamically? One may expect the gas to move (inward) out of the stagnation region as soon as its specific angular momentum is reduced slightly below the local equilibrium value, because of an imbalance of gravity and centrifugal force. If this were true, the amount of angular momentum reduction achievable in the region will be quite limited. However, it takes a finite amount of time for even the full gravity to reaccelerate the material to (say) the sound speed from at rest, no matter how small a value its angular momentum has been reduced to; in many cases, the gravity must first reverse the (slowly) expanding motion often found near the centrifugal barrier, which takes additional time. If the magnetic torque is strong enough, it can remove a large fraction, if not all, of the angular momentum of the gas within that time. In other words, it is the inertia of the stalled gas that enables the magnetic braking to reduce the specific angular momentum significantly below the local equilibrium value. The efficient, localized, braking is responsible for the unique, "hopping," pattern of alternating stagnation and rapid infall seen in Fig. 12.

The rotationally supported rings show up clearly in the density map (Fig. 13). They are overdense regions near the equator created by stalled infall, which leads to a pileup of matter.

The slowdown also allows more time for magnetic braking to operate. The clearest evidence for enhanced braking comes from the outer most ring near the dimensionless radius $x \sim 0.1$: there is an outflow driven from that location at an acute angle with respect to the equatorial plane, as in the magnetic bubble of the standard case. Evidence for braking-driven outflows from the inner two rings is less clean-cut; they may be masked by the chaotic meridianal flow pattern in the puffed-up region outside the equatorial rings. The chaotic motions are generally subsonic. They are dominated in 3D by supersonic rotation. Indeed, the puffed-up structure is equivalent to the magnetic bubble in the standard model: both are supported by a combination of (mostly toroidal) magnetic fields and rotation. In some sense, the puffed-up structure is a collection of (relatively weak) bubbles, driven from multiple centrifugal barriers whose locations vary in time. Such a structure is also present in the somewhat stronger field case of $\lambda = 40$. We believe it is a generic feature of the magnetized rotating collapse when the field is strong enough to disrupt the rotationally supported disk but too weak to channel the outflowing material into a single, coherent bubble. This feature is discussed further in § 6.2.

We note that the number of discrete centrifugal barriers depends on the field strength. As the field strength decreases, more and more centrifugal barriers appear, until they start to overlap and merge into a single, more or less contiguous structure — a rotationally supported disk (see the $\lambda = 400$ case discussed above). Conversely, the disk is replaced by fewer and fewer centrifugal barriers as the field strength increases. For the standard, $\lambda = 13.3$ case, the number of identifiable centrifugal barriers is one at most times. This number can drop to zero for more strongly magnetized cases, to which we turn our attention next.

## 4.2. Relatively Strong Field Cases

We first focus on the time evolution of the central point mass (Fig. 14), which provides an overall measure of the collapse solutions. The point mass at a give time remains similar or even becomes smaller as the field strength increases, unlike the moderately weak field ($\lambda = 80$ to 13.3) cases. The trend is especially clear for the strongest field case of the whole set ($\lambda = 4$). This change in the dependence of point mass on the field strength indicates a change in the solution behavior. In the weak field cases, the mass accretion is limited by angular momentum removal, whose rate generally increases with the field strength. Angular momentum removal is no longer the limiting factor in the strong field cases: the (poloidal) fields at small radii are apparently strong enough, especially after amplification from collapse, that a relatively small twist can remove most of the angular momentum of the collapsing material and redistribute it to large distances. The limiting factor shifts instead to the

magnetic tension, which replaces the rotation as the main impediment to mass accretion. The tension is stronger (relative to gravity) for a smaller mass-to-flux ratio $\lambda$. Indeed, if $\lambda < 1$ (i.e., a magnetically subcritical core), the tension force would prevent core collapse and mass accretion altogether.

Unlike angular momentum, the magnetic flux cannot be removed in the ideal MHD limit that we are working in. It accumulates near the central object — in the central hole in our simulation. The flux accumulation and its sudden release through reconnection allow the magnetic tension to suppress mass accretion onto the central object over an extended period of time even in a magnetically supercritical core with an $\lambda$ significantly larger than unity. They are responsible for the step-like variations of the point mass shown in Fig. 14. Before discussing magnetic reconnection in § 4.2.2, we first consider the collapse solution at a time representative of the conditions before a reconnection event.

### 4.2.1. Removal of Angular Momentum in a Magnetic Braking-Driven Wind

We show in Fig. 15 a snapshot of the $\lambda = 4$ case at a representative time before reconnection. Although one can still divide the collapse solution into four regions as in the standard case (collapsing envelope, equatorial pseudodisk, magnetic bubble and polar funnel, see Fig. 2), these regions are less distinct. In particular, the magnetic bubble (defined as the region where the toroidal field is stronger than the poloidal field) is much less prominent than in the standard $\lambda = 13.3$ case. It is located at a larger distance from the center and contains a much lower mass and angular momentum. Within a radius of $x = 3$, the dimensionless mass of the bubble is only 0.18 and angular momentum is 0.28. These are to be compared with the bubble mass of $\sim 2.3$ and angular momentum of $\sim 1.4$ estimated earlier for the standard case. Indeed, the bubble can be more profitably viewed as part of a broader magnetic braking-driven wind, where the field lines are twisted to varying degrees. The (poloidal) field is strong enough that even a relatively small twist can exert an appreciable torque on the gas: for a fixed twist angle, the magnetic torque is proportional to the field strength squared. Compared to the standard case, the twisted field lines unwind faster because of a higher Alfvén speed. Another difference is the absence of a prominent magnetic wall in which the field lines are severely compressed; the stronger fields are more difficult to compress. As a result, the collapsing envelope merges more smoothly into the equatorial pseudodisk, which is now much thicker. The centrifugal force inside the pseudodisk remains substantially below the gravity in general. In some sense, parcels of infalling material are chasing their centrifugal barriers but unable to reach them because of efficient magnetic braking, which continuously moves the barriers inward. We conclude that the formation of

a rotationally supported disk is completely suppressed in the relatively strong field regime, in agreement with the earlier work of ALS03.

### 4.2.2.   Magnetic Reconnection and Episodic Mass Accretion

A feature not apparent in the early work is episodic mass accretion. As can be seen from Fig. 14, most of the central mass in the $\lambda = 4$ case is accreted in discrete bursts, which are caused by magnetic reconnection. To determine how the bursts are triggered, we focus on the large burst around $t = 9.1 \times 10^{11}$ sec. A snapshot of the inner part of the collapse solution before reconnection is shown in the left panel of Fig. 16. Note the nearly radial field lines that thread the surface of the inner hole. Together with their mirror images (of opposite polarity) in the lower quadrant (not shown), they form a split magnetic monopole. The monopole compresses the material in the equatorial region into a thin, dense (pseudo)disk, which collapse supersonically. As more and more disk material falls into the point mass, more and more field lines are added to the central hole. The growing monopole pushes on the disk material harder and harder from above and below. When field lines of opposite polarities are pressed into a single cell on the equator, they reconnect quickly due to numerical diffusion. We observe a maximum in the magnetic flux that threads the inner hole shortly before the onset of violent reconnection. There is a brief period of time when matter falls into the central hole but not the field lines. The separation indicates that significant magnetic diffusion is present before the violent reconnection. The reconnected field lines pull the disk material outward (see the right panel of Fig. 16), leaving behind an evacuated region that is unable to keep the oppositely directing, monopolar field lines apart. As a result, the field lines threading the central hole rush onto the disk, adding to the reconnected field lines that accelerate the equatorial material outward. Except for a tiny amount of mass falling into the central hole in the polar region, mass accretion is essentially terminated.

As the dense blob (or ring in 3D) shown in the right panel of Fig. 16 moves outwards, it gradually slows down for several reasons. First, it ploughs into infalling material, which cancels some of its outward momentum. Second, as the mass of the blob increases, through both sweeping up material along its path and accretion from above and below along field lines, the gravitational pull of the central point mass increases as well. In addition, the magnetic tension that pushes the blob outwards from behind weakens with time, as the bent field lines straighten up. Sooner or later, there will be enough material accumulated for the gravity to overwhelm the magnetic forces and pull the matter toward the center again. The recollapsing flow in the equatorial region typically moves at a speed well below the local free fall speed, because it has to drag along with it a rather strong magnetic field, which resists

the gravitational pull through tension force.

Once the bulk of the recollapsing material reaches the inner hole, it produces a burst in mass accretion. At the same time, the accreted material deposits its magnetic flux on the surface of the inner hole, creating a growing split magnetic monopole that, in time, would shut off the mass accretion through reconnection, and eject the remaining material to larger distances, starting another cycle of mass accumulation, collapse, and ejection. In some sense, the split monopole acts as an ever tightening "magnetic gate:" as magnetic flux accumulates, mass accretion becomes more and more difficult, until shut off almost completely by reconnection; the reconnection allows a large amount of magnetic flux (associated with the central point mass) to act on a small amount of (disk) matter.

In summary, we have computed the collapse of rotating, strongly magnetized cores with much higher angular resolution at small radii than the previous calculations that employ a cylindrical coordinate system. We confirmed the conclusion of ALS03 that the magnetic braking in such cores is too strong for the rotationally supported disks to form in the ideal MHD limit. We went one step further, showing that the disk suppression holds true even in the presence of (numerically triggered) reconnection. The main effect of the reconnection events is to generate episodic mass accretion.

## 5. Effects of Rotation Speed

The initial rotation speed $v_0 = 0.5$ (in units of sound speed) adopted in the standard simulation is on the high side of the observationally inferred range. Here we discuss three variants of the standard model, with $v_0 = 0$, 0.125 and 0.25, respectively. Without rotation, the collapsing envelope is expected to fall into the central object at a high rate. This is indeed the case, as shown in Fig. 17. The dimensionless point mass quickly approaches a nearly constant value, indicating that the non-rotating collapse is approximately self-similar. There are small oscillations in the point mass, which result from magnetic flux accumulation at the inner hole, as in the standard simulation. This episodic behavior is therefore independent of rotation, in accordance with the interpretation based on reconnection that we advanced in the last section. The value of the dimensionless point mass, $\sim 8$, corresponds to a mass accretion rate that is about 4 times higher than the rate for the collapse of a static SIS (1.95; Shu 1977). The accretion rate decreases as the rotation speed increases, as shown in Fig. 17. For the relatively slowly rotating cases of $v_0 = 0.125$ and 0.25, the point mass started out as high as that in the non-rotating case, but gradually approaches a lower, nearly constant value, indicating that an approximate self-similarity is reached in these cases as well.

To illustrate the effects of rotation on the structure of the magnetized collapsing flow, we show in Fig. 18 a representative snapshot for each of the cases with $v_0 = 0$, 0.125, 0.25 and 0.5. In the absence of rotation, three of the four dynamically distinct regions that we have identified in the standard (rotating) model are clearly present: the polar funnel flow (Region IV), equatorial pseudodisk (region II), and collapsing envelope (Region I). They are separated by a magnetic wall, which divides the outer collapsing envelope from the inner two regions, both of which are dominated by the central split magnetic monopole. This magnetic structure is remarkably similar to the one sketched in Fig. 1 of Galli et al. (2006). Rotation changes the appearance of the collapse solution by inflating a bubble in between the polar funnel and the pseudodisk. It is bounded from outside by the envelope. As one may expect intuitively, the size (mostly the width) of the bubble increases with the initial rotation speed; for the same initial magnetic field, a faster rotation should wind up the field lines more, generating a larger magnetic bubble, as shown in the figure. The difference in the rotation speed does not appear to change the dynamics of the core collapse and magnetic braking fundamentally, however.

## 6.   Discussion

### 6.1.   Characteristic Mass-to-Flux Ratio for Significant Magnetic Braking

Our most important result is that the rotationally supported disk can be disrupted by a weak magnetic field corresponding to a mass-to-flux ratio $\lambda \gg 1$. This result may seem surprising at the first sight, in view of the general expectation that the field is dynamically important only when $\lambda \lesssim 1$. To illuminate the reason behind this seemingly unexpected result, we provide an order-of-magnitude estimate of the characteristic mass-to-flux ratio for significant magnetic braking from the following equation:

$$M_d l_d \sim \frac{|B_\varphi| B_z \varpi_d}{4\pi} \left(2\pi \varpi_d^2\right) t, \tag{19}$$

where $M_d$, $l_d$ and $\varpi_d$ are the mass, specific angular momentum and radius of the disk in the absence of magnetic braking at time $t$, and $B_\varphi$ and $B_z$ are the toroidal and vertical components of the magnetic field on the disk surface. The equation is simply a condition on the rate of magnetic braking that would be required to remove all of the disk angular momentum within the time $t$.

The disk mass $M_d$ is related to the magnetic flux threading the disk, $\pi \varpi_d^2 B_z$, through the dimensional mass-to-flux ratio $\lambda/(2\pi G^{1/2})$, which is conserved along any field line during the core collapse in the ideal MHD limit. Eliminating $B_z$ in terms of $M_d$ and $\lambda$ from equation

(19), we have

$$\lambda^2 \sim 2 \left( \frac{|B_\varphi|}{B_z} \right) \left( \frac{GM_d t}{l_d \varpi_d} \right). \tag{20}$$

To simplify the right hand side of the equation further, we assume that the disk is self-gravitating and rotationally supported (as in the $\lambda = 400$ case shown in Fig. [10]), with a rotation speed $v_d \sim (GM_d/\varpi_d)^{1/2}$ and specific angular momentum $l_d \sim v_d \varpi_d$. The above equation then becomes

$$\lambda^2 \sim 4\pi \left( \frac{|B_\varphi|}{B_z} \right) \left( \frac{t}{p} \right), \tag{21}$$

where $p = 2\pi \varpi_d/v_d$ is the disk rotation period.

Clearly, the characteristic mass-to-flux ratio can greatly exceed unity for two reasons: (1) tight wrapping of the disk magnetic field, $|B_\varphi| \gg B_z$, which increases the rate of angular momentum removal through magnetic braking ($\propto |B_\varphi| B_z$), and (2) long braking time compared to the disk rotation period, $t \gg p$. The braking time $t$ can be identified with the time for core collapse.

The two factors are not entirely independent of each other. Since the toroidal magnetic field is created out of the poloidal field by rotation, the field line is expected to become increasingly more twisted with time. Indeed, it may not be unreasonable to approximate the magnetic twist by the number of turns that the disk has rotated around the center within time $t$, so that

$$\frac{|B_\varphi|}{B_z} \sim \frac{t}{p}. \tag{22}$$

In this case, the characteristic mass-to-flux ratio reduces to

$$\lambda \sim 2\sqrt{\pi} \left( \frac{t}{p} \right). \tag{23}$$

To obtain concrete numbers, let us consider a disk formed at time $t$ out of a singular isothermal toroid with an (angle-averaged) initial mass distribution $M(r) = 2(1 + H_0)a^2 r/G$ and spatially constant rotation speed $V_0$. Suppose, as in the case of SIS (Shu 1977), half of the mass within a radius $r = at$ falls into the collapsed object, the disk, at any given time $t$. In this case, the disk mass $M_d \sim (1 + H_0)a^3 t/G$ and specific angular momentum $l_d \sim V_0 at/2$, yielding a disk radius

$$\varpi_d \sim \frac{l_d^2}{GM_d} \sim \frac{V_0^2 t}{8(1 + H_0)a}, \tag{24}$$

and rotation period

$$p \sim \frac{\pi}{4(1 + H_0)^2} \left( \frac{V_0}{a} \right)^3 t. \tag{25}$$

Substituting equation (25) into equation (23), we finally have

$$\lambda \sim \frac{8(1+H_0)^2}{\sqrt{\pi}} \left(\frac{a}{V_0}\right)^3. \tag{26}$$

For the initial mass distribution with $H_0 = 0.4$ and rotation speed $V_0 = 0.5a$ adopted in § 4, we obtain a characteristic mass-to-flux ratio for significant magnetic braking of $\lambda \sim 70$. This number is remarkably close to our numerically determined value for the disk disruption to begin, which is around 100. Given the crudeness of the estimate, the agreement is encouraging. The analytic estimate brings out the key ingredient for efficient disk braking by even weak magnetic fields: short disk rotation period compared to the core collapse time. In addition, it indicates that the disk in a more slowly rotating core can be disrupted by a weaker magnetic field, which makes physical sense.

Besides the rotation rate, another factor that may also affect the value of the mass-to-flux $\lambda$ for significant magnetic braking is (non-axisymmetric) gravitational torque. The torque can speed up mass accretion through a self-gravitating disk, shortening the time available for field line wrapping and magnetic braking. This additional means of angular momentum redistribution is expected to decrease the efficiency of magnetic braking somewhat. To fully quantify this effect, high resolution 3D simulations are required. Our 2D (axisymmetric) calculations, while idealized in several ways (see § 6.4 below), allow us to concentrate on the role of magnetic braking in disk dynamics without extra complications from gravitational torques and fragmentation. We believe the basic conclusion that even weak magnetic fields with $\lambda \gg 1$ are dynamically important in disk formation and evolution is robust.

## 6.2. Magnetogyrosphere

Surrounding the strongly braked disk is a vertically extended structure where the bulk of the angular momentum of the material collapsed from the envelope is parked. The structure is supported by a combination of (toroidal) magnetic field and rotation. We term it "magnetogyrosphere," to distinguish it from the purely magnetically dominated "magnetosphere" or the rotationally supported disk.

An example of the magnetogyrosphere is shown in Fig. 13, where $\lambda = 80$. In this particular case, the collapsing envelope material is channeled by the magnetic wall surrounding the magnetogyrosphere into the equatorial region, where the infalling material crosses multiple centrifugal barriers on its way to the center. The braking of the equatorial material, particularly at the multiple centrifugal barriers, is what powers the rather chaotic motions inside the slowly expanding magnetogyrosphere. The dimensionless size of the magnetogyrosphere

is $\sim 0.25$, corresponding to a physical size of $\sim 10^3$ AU at a time of $2 \times 10^{12}$ sec, for a sound speed of $a = 0.3$ km/s. By this time, the central point mass is about 0.3 M$_\odot$, whereas the mass of the magnetogyrosphere is about 1.1 M$_\odot$ within $10^3$ AU of the origin (we ignore the rotating, outflowing region near the axis at larger distances that contains relatively little mass). Most of the material collapsed from the envelope is therefore stored in the magnetogyrosphere, rather than going into the central object. It is prevented from falling into the center by the combined effect of magnetic field and rotation. To be quantitative, the mass weighted flow speed in the poloidal plane is only 0.13 km/s inside the magnetogyrosphere, which is less than half of the sound speed $a = 0.3$ km/s. This is consistent with the fact that the size of the magnetogyrosphere is increasing slowly, at a rate of roughly a quarter of the sound speed. For comparison, the free fall speed $V_{\mathrm{ff}} = [2GM(r)/r]^{1/2}$ at the outer edge of the magnetogyrosphere at $10^3$ AU is 1.55 km/s, an order of magnitude higher than the average poloidal speed. The bulk of the magnetogyrospheric material is levitated against the gravity by a combination of (mostly magnetic) pressure gradient and centrifugal force from rotation; the mass averaged rotation speed is 1.23 km/s, not far from the free fall speed.

Qualitatively similar behaviors are found in other moderately weakly magnetized models of $\lambda = 40$, 20, and 13.3. For example, in the standard model with $\lambda = 13.3$, the magnetic braking is strong enough that only a single centrifugal barrier exists. After exiting the barrier, the equatorial material falls straight to the center whereas the extracted angular momentum is stored in a slowly expanding bubble — the magnetogyrosphere, an extended structure again dominated by a combination of magnetic field and rotation (see § 3.2). Compared with the $\lambda = 80$ case, the magnetogyrosphere contains less material (with a mass somewhat less than, rather than well exceeding, the central mass), which moves faster on average and in a more ordered fashion in the poloidal plane.

To illustrate what the magnetogyrosphere may look like observationally, we show in Fig. 19 the column density distributions of the $\lambda = 80$ and 13.3 viewed perpendicular to the axis. In both cases, there is a highly-flattened, dense equatorial region, sandwiched by a more puffed-up structure. The former may potentially be mistaken for a rotationally-supported equilibrium disk around the central object; in reality, it is a highly dynamic structure that collapses supersonically and rotates significantly below the local equilibrium rate at most radii, except near the centrifugal barrier(s). The latter is the slowly expanding magnetogyrosphere. It is held up mostly by the (toroidal) magnetic field in the vertical direction and laterally by rotation.

### 6.2.1. Connection to Observations: IRAM 04191 and HH 211

Magnetogyrospheres should exist in some form. Fundamentally, this is because a rotating, collapsing core will necessarily develop a differential rotation, which inevitably interacts strongly with a poloidal magnetic field, as long as the matter and field are well coupled. The interaction is especially strong near the centrifugal barrier, where the slowdown of infall motion allows more time for the differential rotation to wrap up the field lines. When the field is strong enough to remove angular momentum from the collapsing material, but too weak to transport most of the removed angular momentum out of the system, a magnetogyrosphere develops. In principle, the magnetogyrosphere can be distinguished easily from the collapsing (inner) envelope, since both the velocity and magnetic field are dominated by the toroidal component in the former and by the poloidal component in the latter. They also have different volume and column densities, which may also help separating the two. In practice, the mass distribution and especially the kinematics of both the magnetogyrosphere and the inner envelope are expected to be modified by the powerful protostellar winds, which sweep the ambient medium into bipolar molecular outflows. To search for observational evidence for the magnetogyrosphere, the best place to start may be those Class 0 sources that have relatively narrow molecular outflows.

One of the best studied Class 0 sources is IRAM 04191. The source has a low luminosity of $\sim 0.1\, L_\odot$ (André, Motte, & Bacmann 1999; Dunham et al. 2006), which points to a central stellar object of mass perhaps no more than $0.1\, M_\odot$. The object is surrounded by an extended envelope of mass $\sim\ 0.5 M_\odot$ within a radius of 4200 AU, estimated from dust continuum emission (André et al. 1999). Molecular line observations have established that the envelope is both infalling and differentially rotating (Belloche et al. 2002). It is well traced by $N_2 H^+$, except close to the center, where the molecule appears to be depleted (Belloche & André 2004). Lee, Ho, & White (2005) found that the $N_2 H^+$ envelope consists of two kinematically distinct parts: a fluffy outer region and a dense inner structure that resembles a thick, clumpy, tilted ring. The thick ring-like structure has an average radius $r_0 \sim 1400\ AU$ (or $10''$). The most puzzling, and potentially the most revealing, kinematic feature is the inferred infall speed at the radius $r_0$: $v_r(r \sim r_0) \sim 0$. The small radial speed implies a pileup of infall material, and may have created the dense ring in the first place. The stagnation of infall, if confirmed, would have strong implications for the dynamics of mass accretion and angular momentum evolution. It may mark the transition from the collapsing envelope to a circumstellar structure dominated by magnetic fields and rotation — the magnetogyrosphere in our picture.

Rotation alone can in principle stop the observed infalling envelope at the radius $r_0$, as would be the case near a centrifugal barrier. The rotation speed at $r_0$ is estimated to

be $V_{\varphi,0} \sim 0.16$ km/s, corresponding to a centrifugal force $V_{\varphi,0}^2/r_0 \sim 1.22 \times 10^{-8}$ cm/s$^2$ per unit mass. It is to be compared with the gravitational acceleration $G[M_{\mathrm{env}}(r_0) + M_*]/r_0^2 \sim 7.56 \times 10^{-8}$ cm/s$^2$, where we have assumed 0.1 M$_\odot$ for the central stellar mass and 0.15 M$_\odot$ for the mass within $r_0 = 1400$ AU (out of the estimated $\sim 0.5$ M$_\odot$ within 4200 AU). The ratio of gravitational to centrifugal forces is therefore $\sim 6$, although it may be lower by perhaps up to a factor of 2 due to uncertainties in the mass estimates. In any case, the inferred rotation does not appear to be faster enough to counter the gravity (Lee et al. 2005), which implies that the stagnation point $r_0$ is not a centrifugal barrier. This result is consistent with the constraint that an optically thick disk, if exists at all, must be smaller than 10 AU (Belloche et al. 2002), well inside the stagnation radius $r_0$.

The infalling envelope can also be stopped at the magnetic barrier. The barrier is a general feature produced by the poloidal magnetic field lines draping over the outer surface of the magnetogyrosphere (see Fig. 2 and Fig. 13). The field lines channel the envelope material towards the equator, where it is slowed down temporarily, before recollapsing towards the center. In the case of IRAM 04191, there is evidence that the material interior to the stagnation radius $r_0$ is moving inwards at a speed comparable to the sound speed (Lee et al. 2005). The rapid infall implies that there is not enough angular momentum to hold up the material by rotation. Indeed, there is some hint that the region interior to $r_0$ rotates more or less as a solid body, which would point to a strong braking, as expected in a magnetic barrier, where the field is strong and the slowdown of infall allows more time for the magnetic braking to operate. The braking is apparently so efficient that an optically thick disk does not form until within 10 AU of the central object, if at all (Belloche et al. 2002).

If strong magnetic braking is indeed operating inside the stagnation radius $r_0$ of IRAM 04191, where is the bulk of the extracted angular momentum deposited? One possibility is the slowly outflowing region (with radial speeds of order 0.4 km/s) that shows up in the position-velocity diagram along the minor axis of the ring-like $N_2H^+$ structure (Lee et al. 2005). This region could be part of the magnetogyrosphere. Alternatively, it could be material accelerated outwards by the fast protostellar wind (Lee et al. 2005). The ambiguity illustrates one of the observational challenges in probing the magnetogyrosphere directly; it may easily be masked by the wind-driven motions. This problem may be alleviated using molecules that are little affected by wind-interaction. Another complication in direct probing of the magnetogyrosphere is the depletion of molecules onto dust grains. Even though $N_2H^+$ is among the last molecules to disappear at high densities (Tafalla et al. 2002), it is heavily depleted close to the central object in IRAM 04191 (Belloche & André 2004; Lee et al. 2005).

In the absence of detailed kinematic information, the morphology of circumstellar material may provide indirect evidence for the magnetogyrosphere. A possible example is

the HH 211 system, the prototype of the class of highly collimated CO molecular outflows (Gueth & Guilloteau 1999; Bachiller & Tafalla 1999). It has a pair of oppositely directing, fast-moving jets, each enclosed by a narrow, slower shell. Recent PdBI observations of the source at a resolution of $0.35''$ reveals that the outer shell is much narrower within about $10^3$ AU of the central object (indeed unresolved transversely, Gueth et al., in preparation). It appears that, as the outflow propagates away from the central region, it is initially confined laterally by a $10^3$ AU-scale structure before suddenly expanding into the more widely open shell-like structure observed at larger distances. A natural possibility for the structure is the magnetogyrosphere, which can provide confinement through both thermal pressure and magnetic "hoop" stresses associated with the toroidal field. Indeed, a glance at the density distribution in Fig. 13 (or Fig. 2) reveals a narrow funnel in the polar region close to the origin where the outflow can plausibly be confined. To strengthen the case for magneto-gyrosphere as the confining structure at the base of the HH 211 molecular outflow, high resolution interferometric observations that probe the kinematics (and ideally the magnetic structure) of the confining structure are needed.

To summarize, there is tantalizing evidence for a magnetic braking-driven magnetogy-rosphere in IRAM 04191 and, to a lesser extent, HH 211. To make a stronger case, more high resolution kinematic data are needed, perhaps from the recently completed CARMA and upgraded PdBI, and especially the upcoming ALMA. A unique model prediction is the existence of more than one centrifugal barriers interior to the magnetic barrier, depending on the field strength and assuming good coupling between the field and matter. Detection of such a feature would clinch the case for disk disruption by (repeated) magnetic braking.

### 6.2.2. Dispersal of Magnetogyrosphere and Late-Time Disk Formation

If the bulk of the angular momentum of the collapsed material is indeed deposited in the magnetogyrosphere, what eventually happens to the magnetogyrosphere becomes an important issue in the angular momentum evolution of the system. We believe the fate of the magnetogyrosphere is tied to that of the dense core material, the majority of which is not incorporated into stars. For example, in the Taurus molecular clouds, the dense $HCO^+$ cores typically contain a few to several solar masses (Onishi et al. 2002), whereas the typical mass of the YSOs is only $\sim 0.5$ $M_\odot$ (Kenyon & Hartmann 1995). It is likely that the bulk of the core material is removed by the powerful protostellar wind (Shu et al. 1987; Matzner & McKee 2000). Since the specific angular momentum of the core material tends to increase with distance, it follows that the protostellar wind blows away the majority of not only the mass, but also the angular momentum, of the system, independent of magnetic

braking and magnetogyrosphere formation.

The formation of a magnetogyrosphere in place of a rotationally supported disk can make the wind-stripping of angular momentum potentially more efficient; it should be easier to blow away the more spherical, lower density, magnetogyrosphere than a disk. The dispersal of the magnetogyrospheric material allows the wind to remove the angular momentum associated with not only the portion of the core material that does not collapse into the central object but also the collapsed portion; the latter is parked mostly in the magnetogyrosphere. Wind-stripping is a powerful mechanism of angular momentum removal that deserves close attention.

The total angular momentum retained in a stellar system may be determined to a large extent by the amount of the high specific angular momentum magnetospheric and/or core material that survives the wind-stripping. The left-over material may recollapse towards the center, perhaps forming a rotationally supported disk, which could persist once the massive, slowly rotating envelope that strongly brakes the disk rotation at earlier times has been cleared away. It takes only a small fraction of the mass and angular momentum of a typical dense core to form a minimum solar nebula. Removal of the braking material — the slowly rotating envelope — is one way for the all-important, rotationally supported disk to appear in the collapse of a magnetized core. Another possibility, to be discussed briefly in § 6.4 below, is through nonideal MHD effects, such as ambipolar diffusion.

## 6.3.   Low Plasma-$\beta$ Disks Supported by Rotation

We find persistent, rotationally-supported, equilibrium disks only in the three weakest field cases, with $\lambda = 400$, 200 and 133. These mass-to-flux ratios correspond to initial values of equatorial plasma-$\beta$ of $7.68 \times 10^4$, $1.92 \times 10^4$ and $8.53 \times 10^3$, respectively. One may not expect such weak fields to have any significant effect on the dynamics. However, they are strongly amplified, through both infalling motion and differential rotation. The amplification is so efficient that, even in the weakest field case of $\lambda = 400$, the magnetic pressure dominates the thermal pressure everywhere in the disk (except near the equatorial plane, where the toroidal field is forced to zero by symmetry), especially in the inner part, where the orbital period is shorter. The enormous difference in the plasma-$\beta$ between the disk region and the collapsing envelope is illustrated in Fig. 20, where we plot $\beta$ as a function of radius along a direction 3° away from the midplane. The distribution is similar along other angles, including those far from the midplane, where the amplified field creates a vertically extended, magnetic tower. The base of the tower is a magnetically dominated "corona" that replaces the classical "accretion shock" that bounds the disk in the absence of magnetic fields (e.g.,

Bodenheimer et al. 1990). It can be viewed as a weak version of the magnetogyrosphere; the bulk of the mass and angular momentum of the collapsed material reside in the disk rather than the corona.

The disk magnetic field cannot be amplified indefinitely. Begelman & Pringle (2007) conjectured that the limiting field strength is such that the Alfvén speed $V_A$ roughly equals the geometric mean of the Keplerian speed $V_K$ and the sound speed $a$ of the gas. The conjecture is motivated by the analysis of Pessah & Psaltis (2005), who showed that the growth rate of the magnetorotational instability vanishes when $V_A = (2V_K a)^{1/2}$. It is qualitatively consistent with our finding that the plasma-$\beta$ tends to be lower in the inner part of the disk where the rotation speed is higher. For a quantitative comparison, we plot in Fig. 20 the predicted plasma $\beta$ distribution based on $\beta = 2a^2/V_A^2 = a/V_K$, where $V_K$ is the equilibrium rotation speed shown in Fig. 11. The rough agreement between the predicted and actual distributions lends some support to the conjecture, even though the toroidal field in our simulation is generated mostly by simple twisting of a pre-existing poloidal field, rather than MRI.

The condition for a rotationally supported disk *not* to be affected significantly by magnetic braking in the ideal MHD limit, $\lambda \gtrsim 100$, may be difficult to satisfy in the Galaxy at the present time. For a typical low-mass core, the field strength must be less than $\sim 1$ $\mu$G on the 0.05pc scale. The required strength is well below the median value inferred by Heiles & Troland (2005) for the cold neutral structures of HI gas. A potential exception is the massive cores of molecular clouds, where column densities as high as 1 g cm$^{-2}$ are often inferred (Plume et al. 1997). If their field strength is about 15 $\mu$G or less, the mass-to-flux ratio $\lambda$ would be of order 100 or more. Such a weak field (relative to mass) should not significantly disrupt disk formation, particularly around massive stars that may form in such cores (McKee & Tan 2002), although it can still be amplified to the extent that its pressure dominates the thermal pressure inside the disk, at least in 2D. If the cores are more strongly magnetized, as is the case for the nearest region of ongoing massive star formation OMC1 (Crutcher 1999; Houde 2004), the field may suppress the formation of a rotationally supported disk altogether, as long as it remains well coupled to the matter. In this case, most of the mass would be accreted through a still rotating but rapidly infalling pseudodisk that is strongly braked by magnetic fields. Quantifying this possibility for massive star formation fully would require 3D simulations that include both radiative transfer (e.g., Krumholz, Klein, & McKee 2007) and magnetic fields, as well as a treatment of ionization and magnetic coupling.

## 6.4. Future Directions

We have performed calculations of disk formation in rotating dense cores magnetized to different degrees under a number of simplifying assumptions. These include axisymmetry, ideal MHD, and ignoring protostellar winds. The calculations provide a starting point for future refinements.

The most straightforward refinement is to increase spatial resolution. Higher resolution 2D (axisymmetric) simulations are desirable in the weakest field cases, where rotationally-supported, equilibrium disks are formed. Such disks can evolve through the twisting of a pre-existing, poloidal field dragged into the disk from large distances by collapsing material. The disk evolution can be aided, perhaps even dominated, by MRI. To adequately quantify the role of MRI in driving disk evolution, one need to resolve the fastest growing MRI mode (Hawley & Krolik 2001; Stone & Pringle 2001), whose wavelength decreases as the field weakens. Another straightforward refinement is to relax the mirror symmetry imposed at the equator. We have explored a few cases without the equatorial symmetry, and found qualitatively similar results. They will be discussed in the future along with 3D simulations.

High resolution, global 3D simulations that include both the core and the disk will be a natural, but challenging, extension of our weak field calculations. They are needed for determining the importance of gravitational torques in redistributing the disk angular momentum relative to hydromagnetic stresses (e.g., Fromang et al. 2004), including those arising from possible MRI associated with the dominant, toroidal component of the disk magnetic field that cannot be treated in 2D. 3D calculations are also needed for treating potential (sub-)stellar companion formation through fragmentation (e.g., Banerjee & Pudritz 2006; Machida et al. 2007; Hennebell & Teyssier 2007).

Equally challenging will be detailed treatment of nonideal MHD effects. Such effects have been investigated over the years, most systematically by Nakano and collaborators (e.g., Nakano, Nishi, & Umebayashi 2002), but have yet to be incorporated into multi-dimensional *protostellar* collapse calculations. Particularly vulnerable to non-ideal effects are two prominent features of our relatively strong field cases: the split magnetic monopole near the center and the associated episodic mass accretion. Sharp kinks in field lines (across the midplane), such as those shown in the left panel of Fig. 16, are expected to be smoothed out by nonideal MHD effects (see Shu et al. 2006, for an example). However, there will still be a tendency for the magnetic flux to accumulate at small radii even when realistic nonideal effects are present. Indeed, episodic mass accretion due to repeated flux accumulation and escape can be seen in the nonideal MHD calculations of Tassis & Mouschovias (2005) under the thin-disk approximation.

Whether the deviation from ideal MHD in a collapsing core is strong enough to enable disk formation is uncertain. Krasnopolsky & Königl (2002) investigated the effects of ambipolar diffusion on magnetic braking and disk formation under the self-similar assumption and thin-disk approximation. They showed that rotationally supported disks can indeed form even in strongly magnetized cores, although this is by no means guaranteed. A particular complication is the hydromagnetic accretion shock of C-type produced by the magnetic flux left behind by the mass that has gone into the central object (Li & McKee 1996; Ciolek & Königl 1998). The increase in field strength and decrease in infall speed inside the shock and in the postshock region tend to enhance the magnetic braking (in a manner akin to the quasistatic phase of subcritical cloud evolution, Basu & Mouschovias 1994), whereas the slippage of field lines relative to neutral matter in the azimuthal direction tends to decrease it. Whether there is enough angular momentum left in the accreting material after passing through the C-shock to form an appreciable disk is uncertain, as demonstrated by Krasnopolsky & Königl (2002) semi-analytically in 1D. Numerical study of this problem in 2D is underway (Mellon & Li, in preparation).

Theory of disk formation will be incomplete without a treatment of protostellar wind. It is likely that the wind removes the bulk of not only the mass, but also the angular momentum, of a (low-mass) star forming core, at least for regions like the Taurus clouds, where the typical mass of a core is well above that of a YSO. As discussed in 6.2.2, there is the possibility of late-time disk formation after the wind has stripped away most of the (slowly rotating) envelope that impedes disk formation through magnetic braking. The role of protostellar wind in the evolution of angular momentum in star formation in general and disk formation in particular remains to be quantified. The various refinements outlined above are not mutually exclusive. However, it will be a daunting, if not impossible, task to implement all of them at the same time. Fortunately the calculations can be guided by high resolution observations with increasingly powerful interferometers, especially ALMA.

## 7. Conclusions

We have performed a set of axisymmetric calculations of protostellar collapse phase of star formation in rotating cores magnetized to different degrees, expanding on the work of ALS03. The goal is to determine how magnetic braking affects disk formation in the ideal MHD limit. The main conclusions are:

1. Protostellar disks can be disrupted by weak magnetic fields corresponding to mass-to-flux ratio $\lambda \gg 1$. This is made possible by the tight wrapping of the disk field lines, which increases the rate of magnetic braking, and the long braking time compared with the disk

rotation period. In our illustrative calculations, the disk disruption begins around $\lambda \sim 100$.

2. Magnetic braking disrupts the rotationally supported disk by creating regions of rapid, supersonic collapse in the disk. These regions are separated by one or more centrifugal barriers, where the rapid infall is halt temporarily and the magnetic braking is locally enhanced. The number of centrifugal barriers decreases as the core becomes more strongly magnetized. Multiple centrifugal barriers, if observed, would clinch the case for disk disruption by magnetic braking.

3. Surrounding the strongly braked disk of spatially alternating collapse and stagnation is a vertically extended structure supported by a combination of (toroidal) magnetic field and rotation — a "magnetogyrosphere" — where the bulk of the angular momentum of the collapsed material is stored. The magnetogyrosphere may be detectable interferometrically, although the detection may be complicated by interaction with protostellar winds. We suggest that the wind may play a key role in determining not only the mass but also the angular momentum of a stellar system.

4. Even in the extremely weak field cases of $\lambda \gtrsim 100$, where a rotationally-supported, equilibrium disk is formed in the ideal MHD limit, the magnetic field can still be dynamically important. It can be amplified to the extent that its pressure dominates the thermal pressure both in the disk and its surrounding region, at least in 2D. The field may affect the fragmentation properties of the disk, and seed the MRI, although high resolution 3D simulations are required to fully quantify its dynamical effects.

5. In relatively strongly magnetized cores of $\lambda \lesssim 10$, the disk formation is completely suppressed, and the bulk of the angular momentum of the collapsed material is ejected out of the system via a low-speed, magnetic braking-driven wind, as found previously. A new feature is that the mass accretion on to the central object is highly episodic, because of magnetic reconnection. How this and other behaviors are modified by nonideal MHD effects, particularly ambipolar diffusion, remains to be quantified.

In summary, our calculations have shown that in the ideal MHD limit the magnetic braking is strong enough to prevent the formation of a persistent, rotationally supported, protostellar disk in all but the unrealistically weak field cases. Since disks are observed around many, if not all, young stellar objects, this result presents an interesting conundrum that must be resolved. For such a disk to form in dense cores magnetized to a realistic level, magnetic braking must be weakened one way or another, perhaps through a combination of nonideal MHD effects and protostellar winds. Quantifying these effects should be a major goal of future research in this area.

## REFERENCES

Allen, A., Li, Z.-Y., & Shu, F. H. 2003, ApJ, 599, 363

André, P., Motte, F., & Bacmann, A. 1999, ApJ, 513, L57

Bachiller, R., & Tafalla, M. 1999, in NATO ASIC Proc. 540, The Origin of Stars and Planetary Systems, ed Lada, C. J. and Kylafis, N. D. (Norwell, MA: Kluwer Acad. Pub.), 227

Balbus, S. A., & Hawley, J. F. 1998, Reviews of Modern Physics, 70, 1

Banerjee, R., & Pudritz, R. E. 2006, ApJ, 641, 949

Basu, S., & Mouschovias, T. C. 1994, ApJ, 432, 720

Beckwith, S. V. W., & Sargent, A. I. 1993, in Protostars and Planets III, ed. E. H. Levy & J. Lunine (Tucson:Univ of Arizona Press), 521

Begelman, M. C., & Pringle, J. E. 2007, MNRAS, 375, 1070

Belloche, A., & André, P. 2004, A&A, 419, L35

Belloche, A., André, P., Despois, D., & Blinder, S. 2002, A&A, 393, 927

Bodenheimer, P. 1995, ARA&A, 33, 199

Bodenheimer, P., Yorke, H. W., Rozyczka, M., & Tohline, J. E. 1990, ApJ, 355, 651

Boss, A. P. 1998, in ASP Conf. Ser. 148, Origins, ed. C. E. Woodward, J. M. Shull, & H. A. Thronson, Jr. (San Francisco: ASP), 314

Ciolek, G. E., & Königl, A. 1998, ApJ, 504, 257

Cohl, H. S., & Tohline, J. E. 1999, ApJ, 527, 86

Crapsi, A., Caselli, P., Walmsley, M. C., & Tafalla, M. 2007, A&A, 470, 221

Crutcher, R. M. 1999, ApJ, 520, 706

Crutcher, R. M., & Troland, T. H. 2000, ApJ, 537, L139

Crutcher, R. M., & Troland, T. H. 2007, in IAU Symp. 237, Triggered Star Formation in a Turbulent ISM, ed. B. G. Elmegreen & J. Palous (Cambridge: Cambridge Univ. Press), 141

Dunham, M. M., et al. 2006, ApJ, 651, 945

Evans, C. R., & Hawley, J. F. 1988, ApJ, 332, 659

Fiedler, R. A., & Mouschovias, T. C. 1993, ApJ, 415, 680

Fromang, S., Balbus, S. A., Terquem, C., & De Villiers, J.-P. 2004, ApJ, 616, 364

Fromang, S., Hennebelle, P., & Teyssier, R. 2006, A&A, 457, 371

Galli, D., Lizano, S., Shu, F. H., & Allen, A. 2006, ApJ, 647, 374

Galli, D., & Shu, F. H. 1993, ApJ, 417, 243

Girart, J. M., Rao, R., & Marrone, D. P. 2006, Science, 313, 812

Goodman, A. A., Benson, P. J., Fuller, G. A., & Myers, P. C. 1993, ApJ, 406, 528

Gueth, F., & Guilloteau, S. 1999, A&A, 343, 571

Hawley, J. F., & Krolik, J. H. 2001, ApJ, 548, 348

Heiles, C., & Troland, T. H. 2005, ApJ, 624, 773

Hennebell, P., & Fromang, S. 2007, A&A, submitted

Hennebell, P., & Teyssier, R. 2007, A&A, submitted

Houde, M. 2004, ApJ, 616, L111

Kenyon, S. J., & Hartmann, L. 1995, ApJS, 101, 117

Königl, A. 1991, ApJ, 370, L39

Königl, A., & Pudritz, R. E. 2000, in Protostars and Planets IV, ed. V. Manning, A. Boss, & S. Russell (Arizona: Univ of Arizona Press), 759

Krasnopolsky, R., Königl, A. 2002, ApJ, 580, 987

Krumholz, M. R., Klein, R. I., & McKee, C. F. 2007, ApJ, 656, 959

Lee, C.-F., Ho, P. T. P., & White, S. M. 2005, ApJ, 619, 948

Li, Z.-Y., & McKee, C. F. 1996, ApJ, 464, 373

Li, Z.-Y., & Shu, F. H. 1996, ApJ, 472, 211

Li, Z.-Y., & Shu, F. H. 1997, ApJ, 475, 237

Lizano, S., & Shu, F. H. 1989, ApJ, 342, 834

Lynden-Bell, D. 2003, MNRAS, 341, 1360

Machida, M. N., Inutsuka, S.-i., & Matsumoto, T. 2007, ApJ, submitted

Matzner, C. D., & McKee, C. F. 2000, ApJ, 545, 364

McKee, C. F., & Tan, J. C. 2002, Nature, 416, 59

McKee, C. F., Zweibel, E. G., Goodman, A. A., & Heiles, C. 1993, in Protostars and Planets III, ed. E. H. Levy & J. Lunine (Tucson:Univ of Arizona Press), 327

Mestel, L., & Paris, R. B. 1979, MNRAS, 187, 337

Mouschovias, T. C., & Ciolek, G. E. 1999,in NATO ASIC Proc. 540, The Origin of Stars and Planetary Systems, ed Lada, C. J. and Kylafis, N. D. (Norwell, MA: Kluwer Acad. Pub.), 305

Mouschovias, T. C., & Paleologou, E. V. 1979, ApJ, 230, 204

Myers, P. C. 1995, in Molecular Clouds and Star Formation, ed. C. Yuan & J. You (Singapore: World Scientific), 47

Nakano, T. 1989, MNRAS, 241, 495

Nakano, T., Nishi, R., & Umebayashi, T. 2002, ApJ, 573, 199

Onishi, T., Mizuno, A., Kawamura, A., Tachihara, K., & Fukui, Y. 2002, ApJ, 575, 950

Pessah, M. E., & Psaltis, D. 2005, ApJ, 628, 879

Plume, R., Jaffe, D. T., Evans, N. J., II, Martin-Pintado, J., & Gomez-Gonzalez, J. 1997, ApJ, 476, 730

Shu, F. H. 1977, ApJ, 214, 488

Shu, F. H., Galli, D., Lizano, S., & Cai, M. 2006, ApJ, 647, 382

Shu, F. H., Adams, F. C., & Lizano, S. 1987, ARA&A, 25, 23

Shu, F. H., Najita, J. R., Shang, H., & Li, Z.-Y. 2000, in Protostars and Planets IV, ed. V. Manning, A. Boss, & S. Russell (Arizona: Univ of Arizona Press), 789

Stone, J. M., & Norman, M. L. 1992, ApJS, 80, 753

Stone, J. M., & Norman, M. L. 1992, ApJS, 80, 791

Stone, J. M., & Pringle, J. E. 2001, MNRAS, 322, 461

Tafalla, M., Mardones, D., Myers, P. C., Caselli, P., Bachiller, R., & Benson, P. J. 1998, ApJ, 504, 900

Tafalla, M., Myers, P. C., Caselli, P., Walmsley, C. M., & Comito, C. 2002, ApJ, 569, 815

Tassis, K., & Mouschovias, T. C. 2005, ApJ, 618, 783

Terebey, S., Shu, F. H., & Cassen, P. 1984, ApJ, 286, 529

Tomisaka, K. 1998, ApJ, 502, L163

Ziegler, U. 2005, A&A, 435, 385
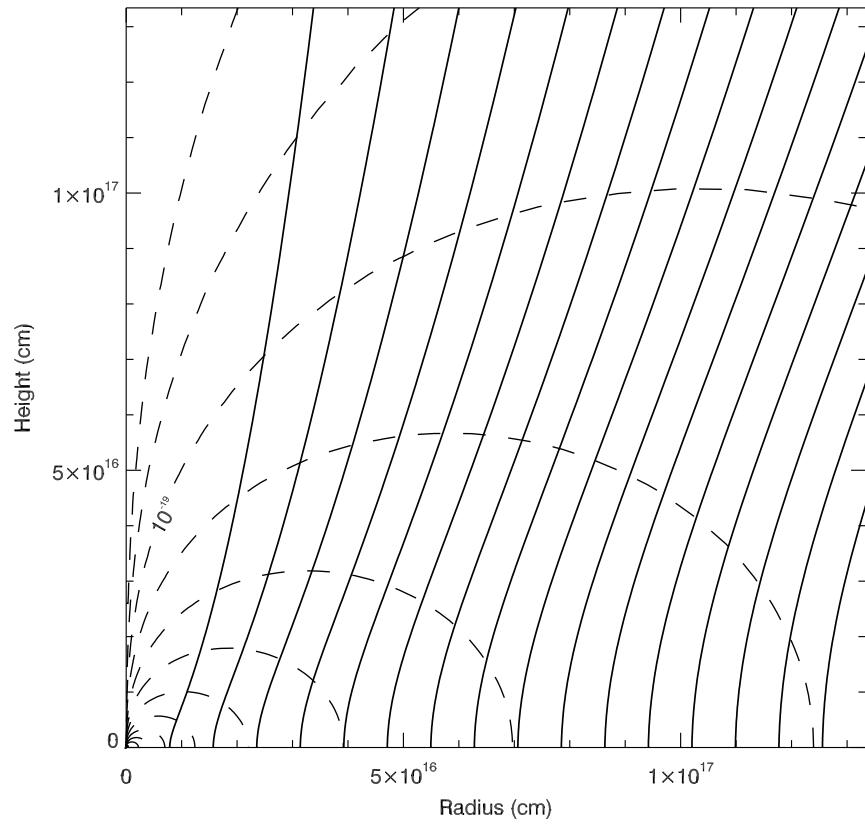
Fig. 1.— Rotating, magnetized singular isothermal toroid (SIT) as the initial configuration for collapse calculation. Plotted are the isodensity contours (dashed lines, with two contours per decade and $10^{-19}$ g cm$^{-3}$ labeled) and the lines of magnetic field (solid).
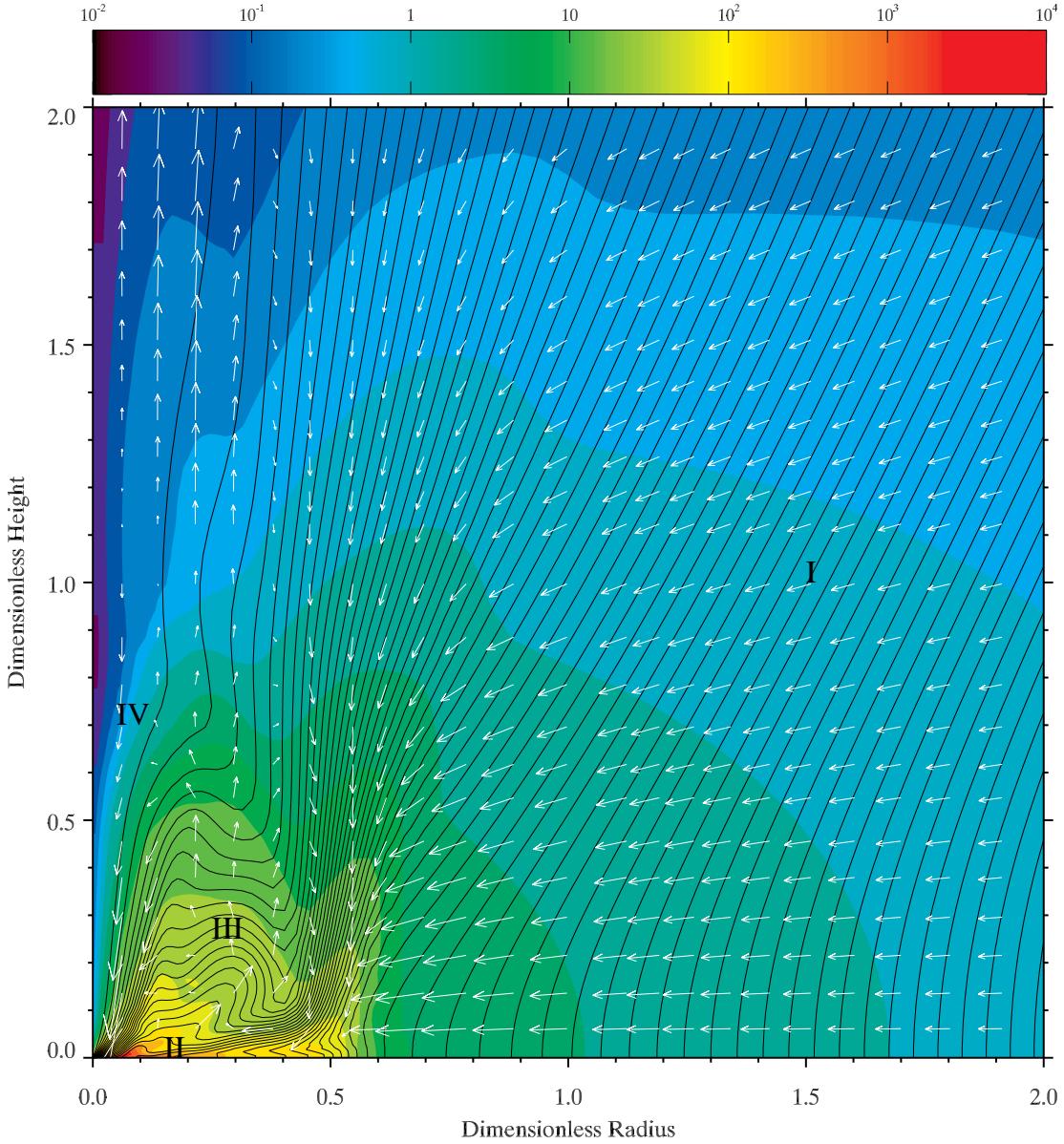
Fig. 2.— Snapshot of the standard collapse solution at a representative time. Shown in color is the distribution of dimensionless density in the meridian plane, with the lines of magnetic field and velocity vectors superposed. The four dynamically distinct regions are labeled, corresponding to the collapsing envelope (Region I), equatorial pseudodisk (II), magnetic bubble (III) and polar funnel (IV). See the text for discussion.
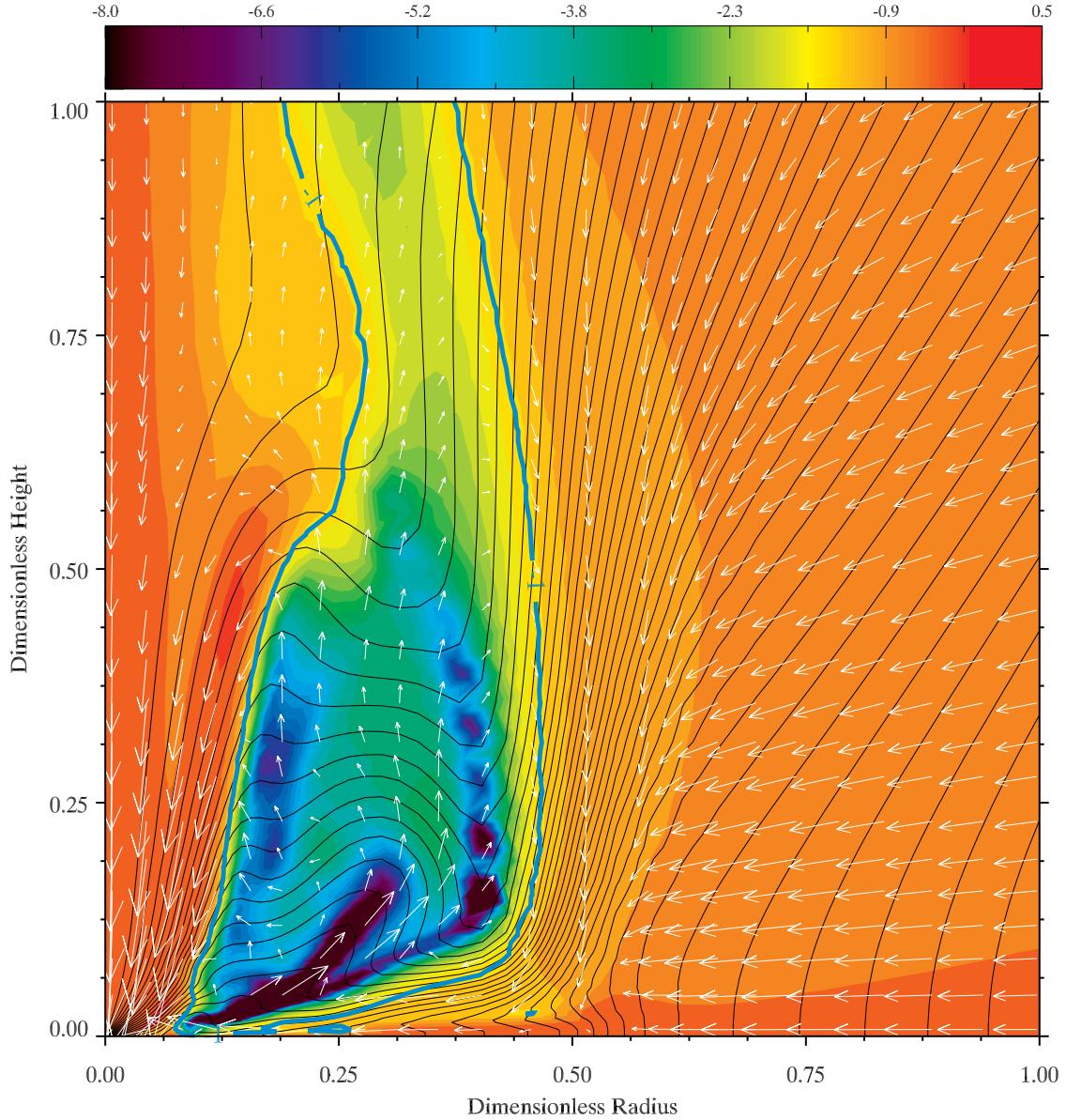
Fig. 3.— Map of the magnetic twist. Superposed on the map are the lines of magnetic field (black) and velocity vectors (arrows). The toroidally dominated magnetic bubble (enclosed within the blue contour labeled with "-1") is surrounded by the polar funnel flow to the left, collapsing envelope to the right, and equatorial pseudodisk from below.
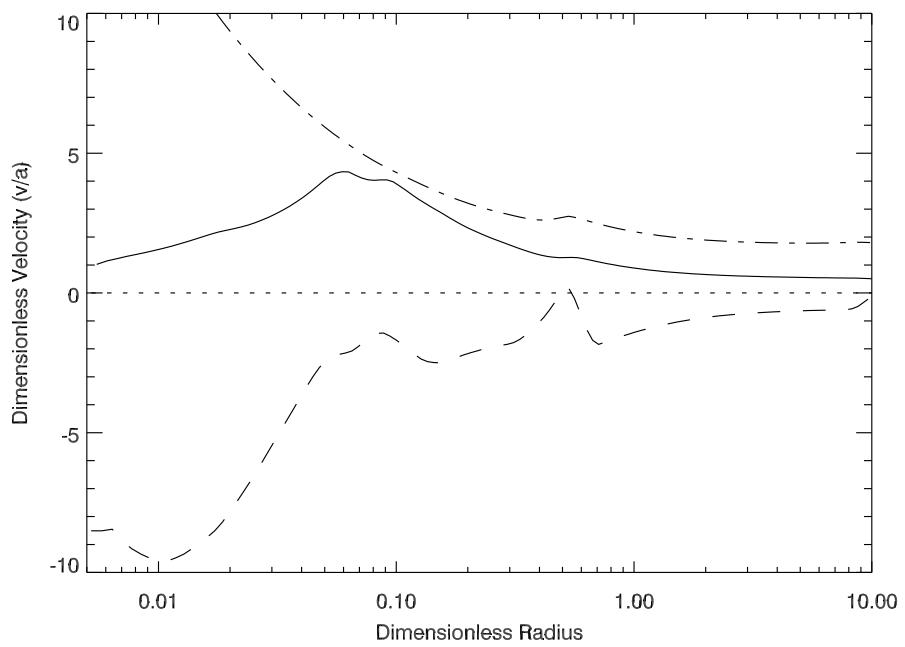
Fig. 4.— Velocity distribution of the standard model on the equator. Plotted are the radial (dashed), rotational (solid) speeds of the fluid, and the rotation speed needed for support against gravity (dot-dashed).
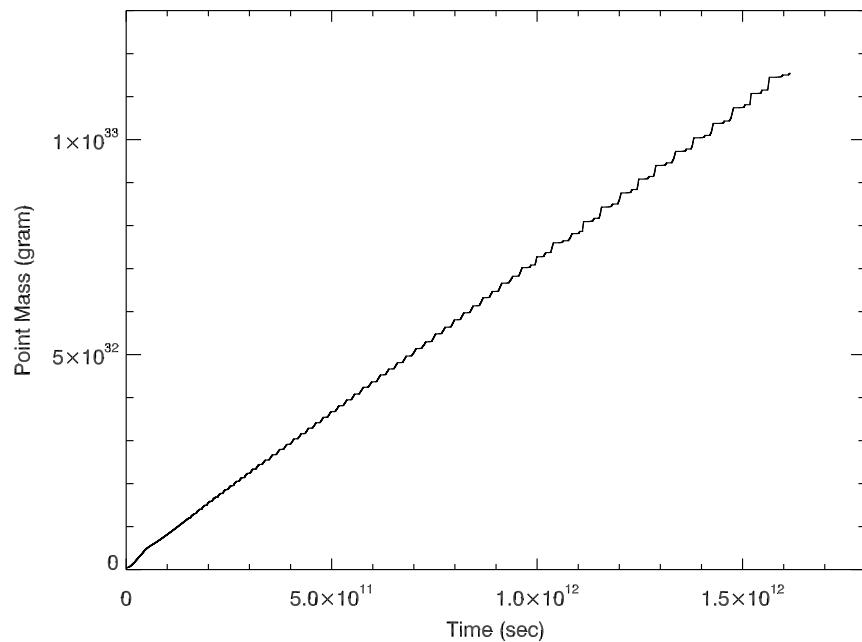
Fig. 5.— Evolution of the central point mass for the standard model. The nearly linear increase of the mass with time indicates that the collapse solution is approximately self-similar.
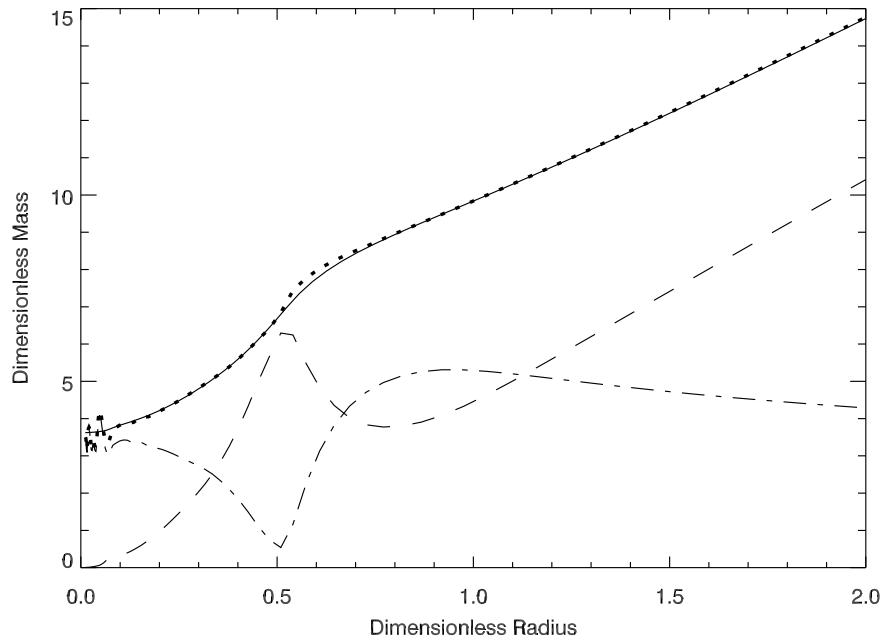
Fig. 6.— Time averaged distributions of the dimensionless mass $m(x)$ enclosed within an expanding sphere of fixed dimensionless radius $x$, computed in two different ways, using eqs (9) (solid line) and (11) (dotted). The averaging is done between $3.0 \times 10^{11}$ and $7.5 \times 10^{11}$ sec. The agreement between the two curves is an indication that the collapse solution is approximately self-similar. Also plotted are the two terms on the right hand side of eq. (11), showing the mass change due to volume expansion (dashed line) and mass crossing the sphere (dot-dashed).
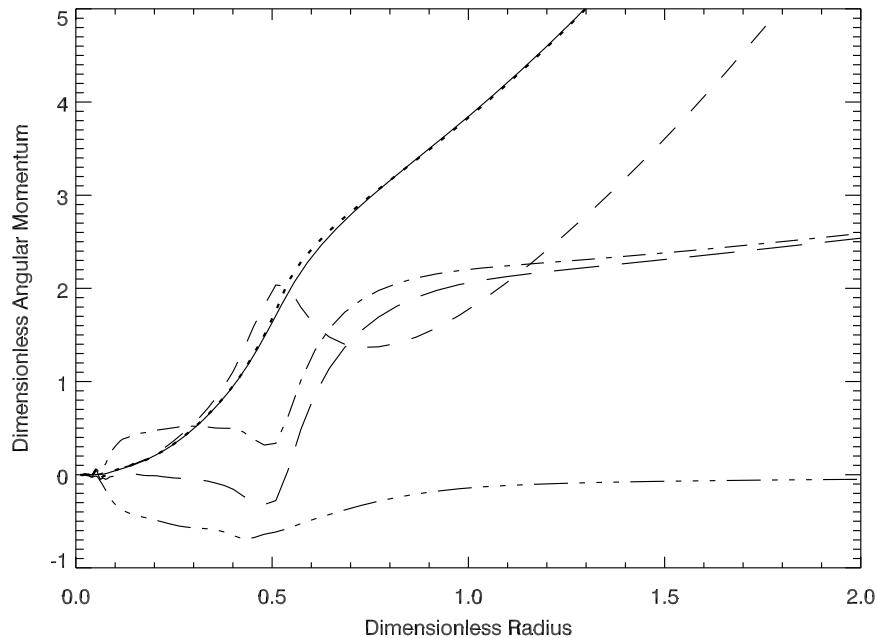
Fig. 7.— Time averaged distributions of the dimensionless angular momentum $l(x)$ enclosed within an expanding sphere of fixed dimensionless radius $x$, computed in two different ways, using eqs. (14) (solid line) and (16) (dotted). The averaging is done between $3.0 \times 10^{11}$ and $7.5 \times 10^{11}$ sec. Also plotted are the three terms on the right hand side of eq. (16), showing the angular momentum change due to volume expansion (dashed), mass crossing the sphere (dot-dashed), and magnetic braking (dot-dot-dashed). The sum of the last two terms is plotted as the long dashed line, showing that the angular momentum advected into a sphere of radius $x \lesssim 0.4$ by fluid motion is almost completely removed by magnetic braking.
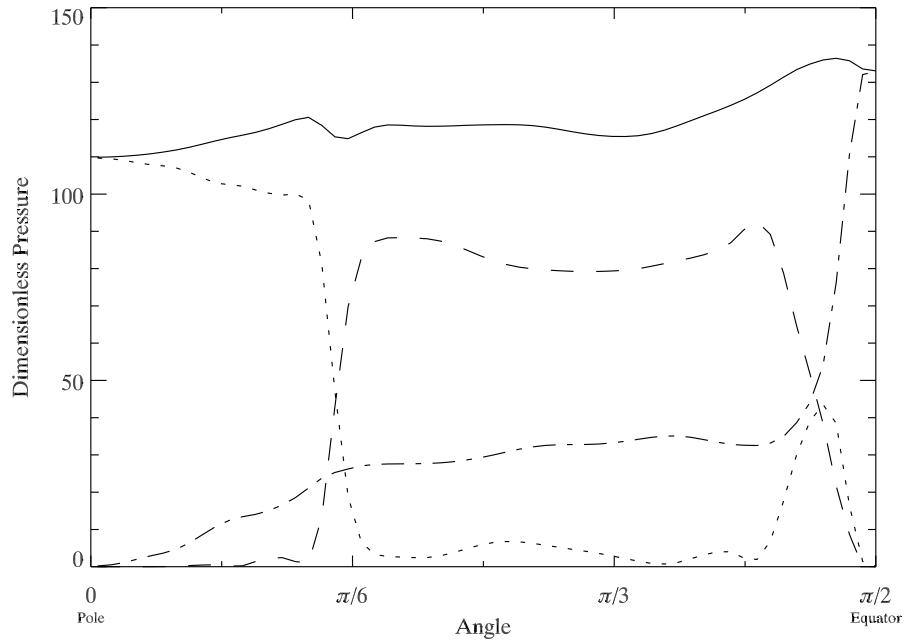
Fig. 8.— Time averaged angular distributions of the total pressure and its components at a representative radius $x = 0.3$ for the standard case. The total pressure (solid line) is nearly constant in $\theta$, but is dominated by different components in different regions. The thermal pressure (dot-dashed) dominates in the pseudodisk, the toroidal magnetic pressure (dashed) dominates in the bubble, and the poloidal magnetic pressure (dotted) dominates in the polar region.
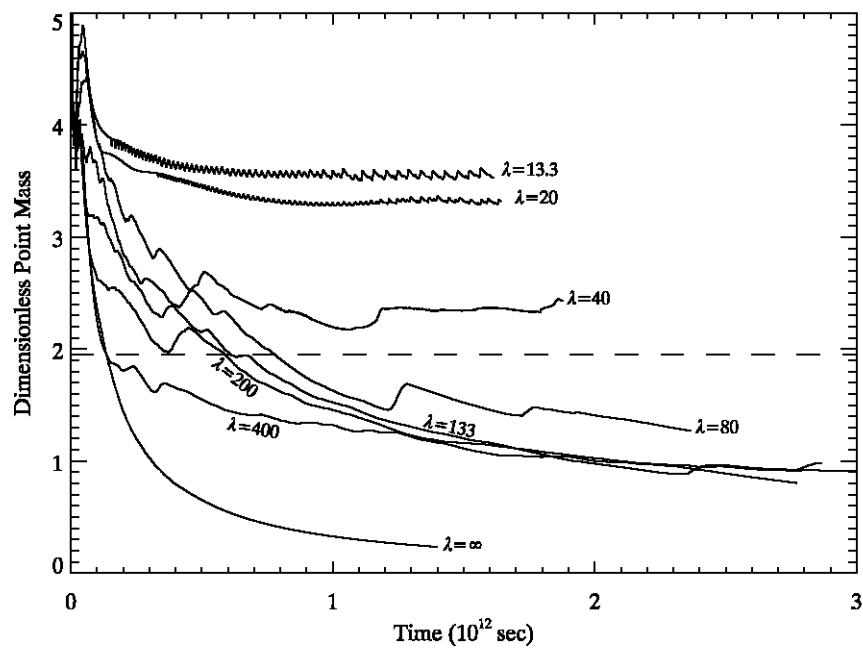
Fig. 9.— Time evolution of dimensionless point mass for relatively weak magnetic field cases. The mass-to-flux ratio increases from the standard model ($\lambda = 13.3$) on the top to the non-magnetized case ($\lambda = \infty$) on the bottom.
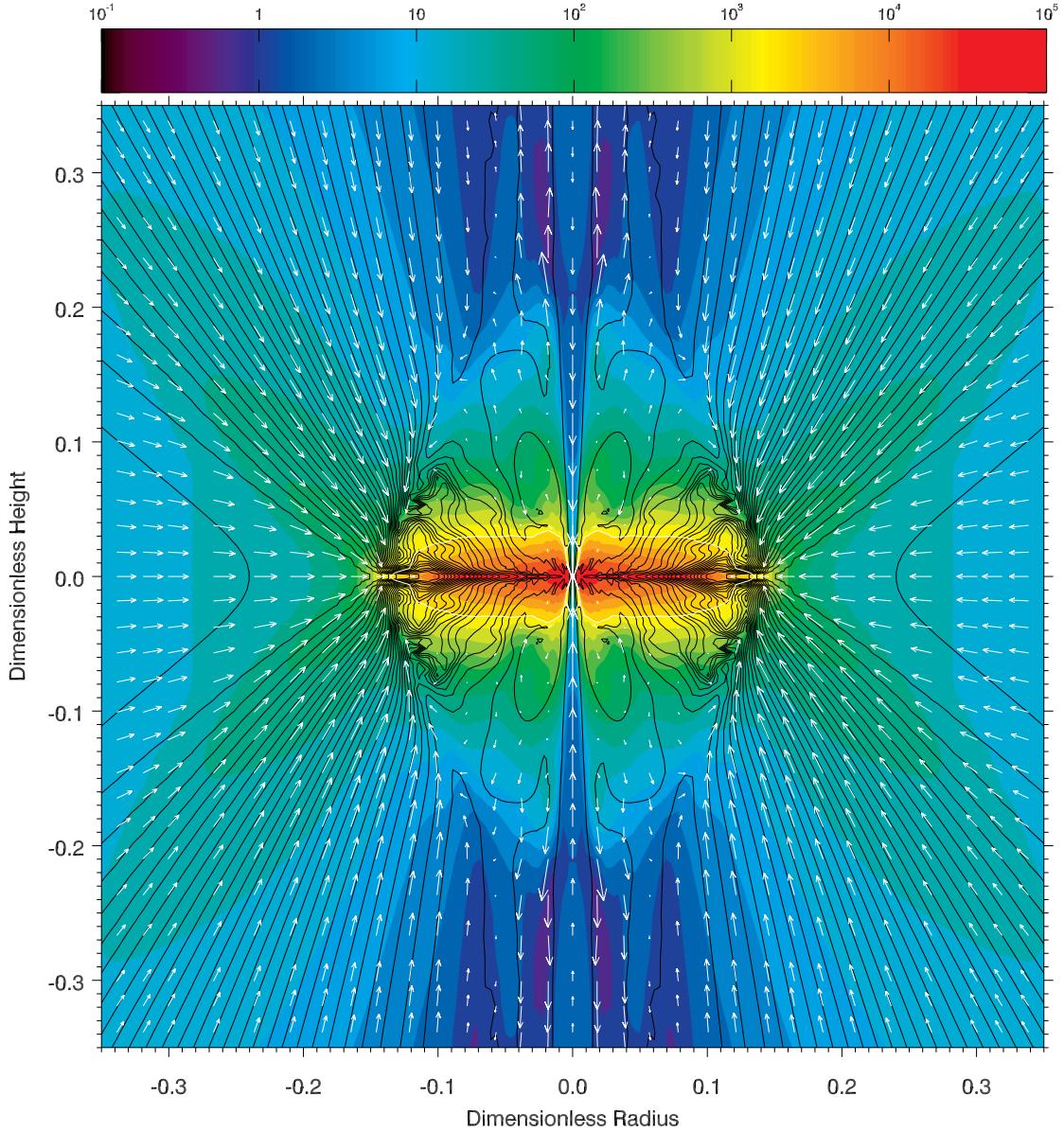
Fig. 10.— A snapshot of the disk formed in the weakest field case of $\lambda = 400$. The density is plotted in color contours, with the magnetic fields lines in black and the velocity field as white arrows. The dimensionless density of $3 \times 10^3$ (white contour) provides a fiducial boundary for the disk.
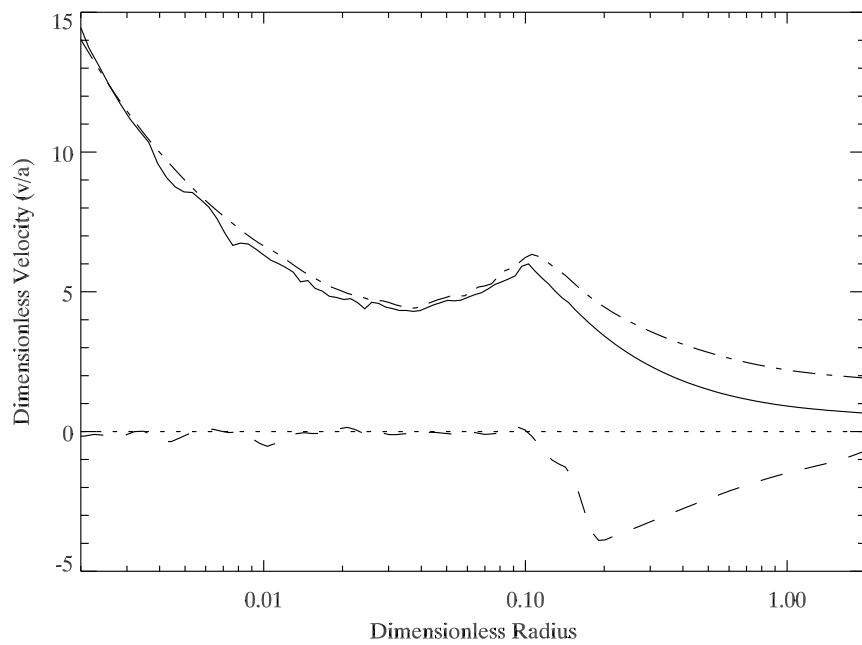
Fig. 11.— Infall (dashed line) and rotation (solid) speeds on the equator at the representative time for the weakest field case of $\lambda = 400$. The rotational support for the disk is seen by comparing the rotation speed to the equilibrium value (dot-dashed), and by the corresponding drop in the infall speed.
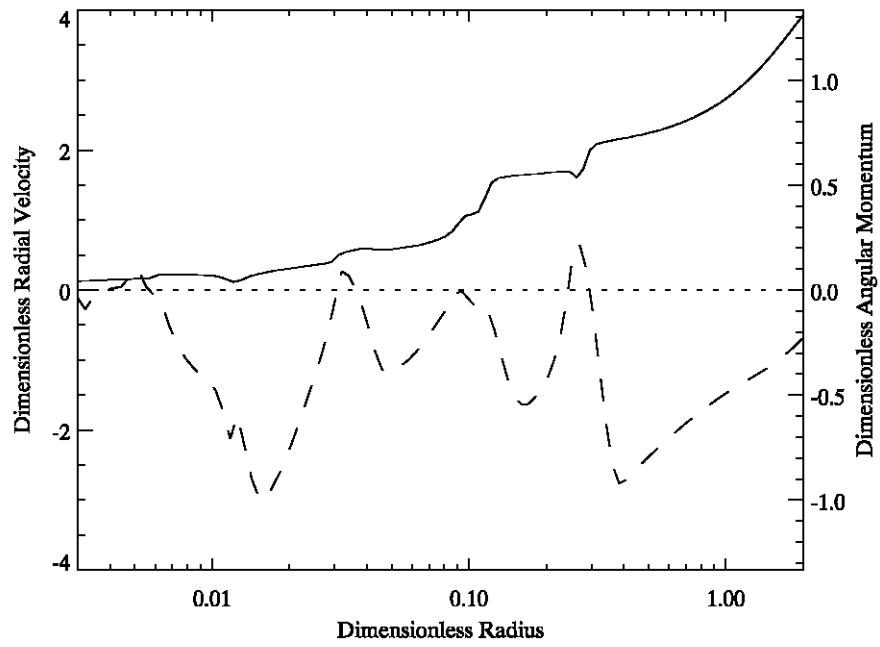
Fig. 12.— Radial velocity (dashed curve) and specific angular momentum (solid) on the equator at a representative time $t = 2 \times 10^{12}$ sec for the relatively weak field case of $\lambda = 80$. They are in units of, respectively, the sound speed $a$ and $a^2 t$. Note the abrupt drops in angular momentum at the stagnation points of the collapsing flow.
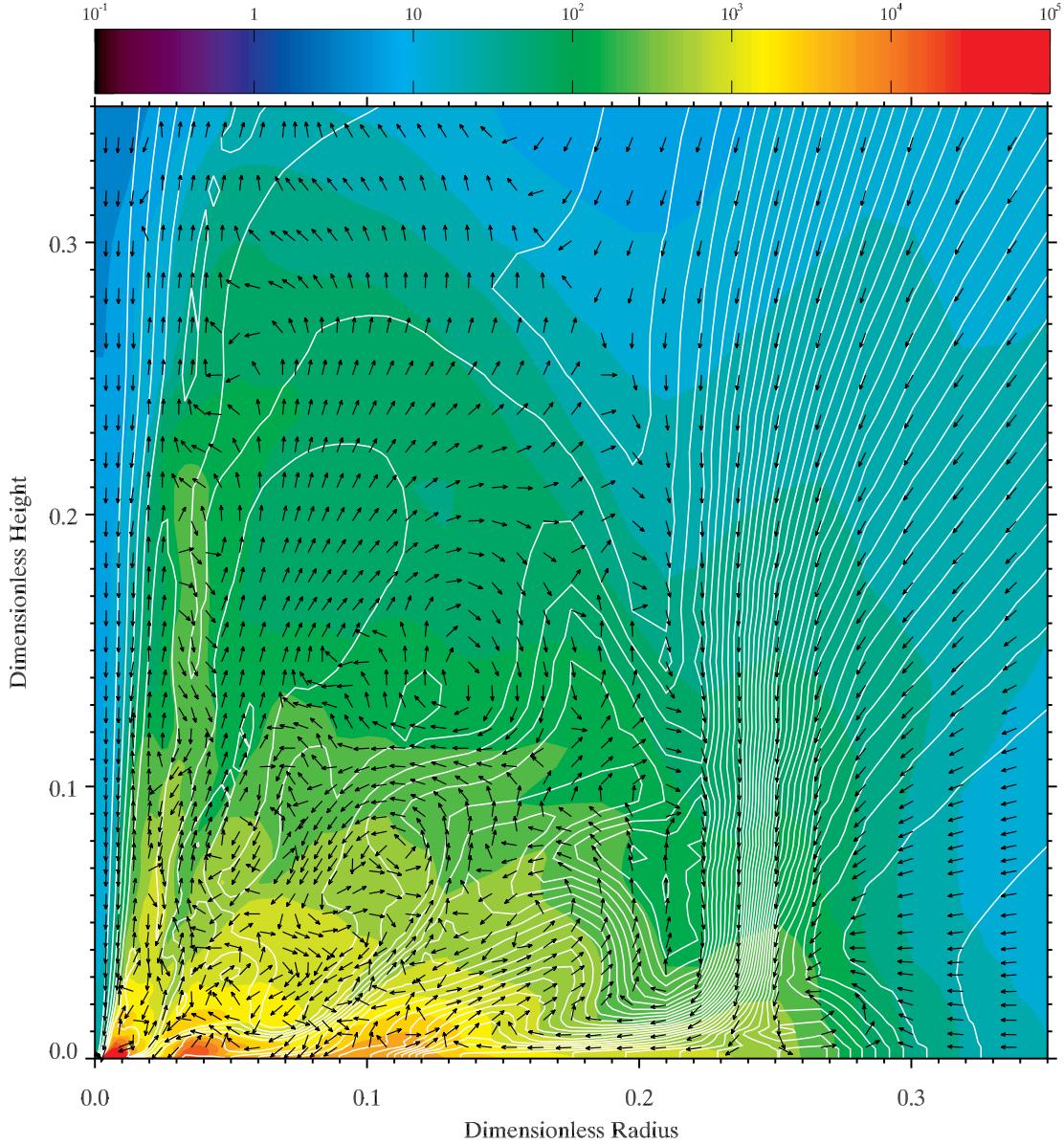
Fig. 13.— Map of density distribution in a transition case ($\lambda = 80$), at the representative time. Transient high density rings form instead of a disk as infalling material piles up near centrifugal radii, then recollapses after losing a large fraction of its angular momentum through magnetic braking. White contours are magnetic field lines, and arrows are unit velocity vectors.
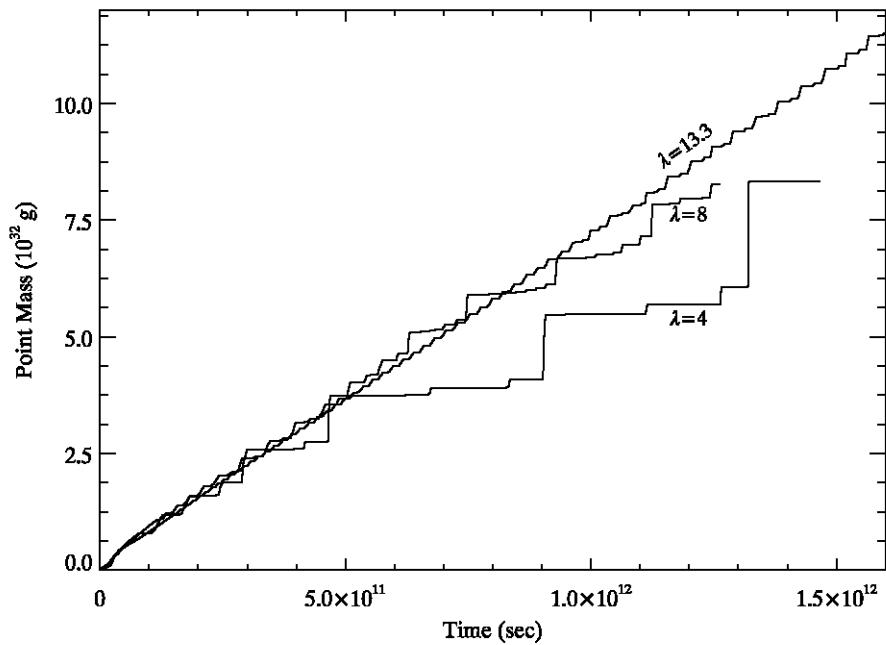
Fig. 14.— Time evolution of dimensionless point mass for relatively strong magnetic field cases. The mass-to-flux ratio decreases from top to bottom, the opposite of the trend seen in the low field cases. Note the step-like behavior, especially in the highest field case, indicative of episodic mass accretion.
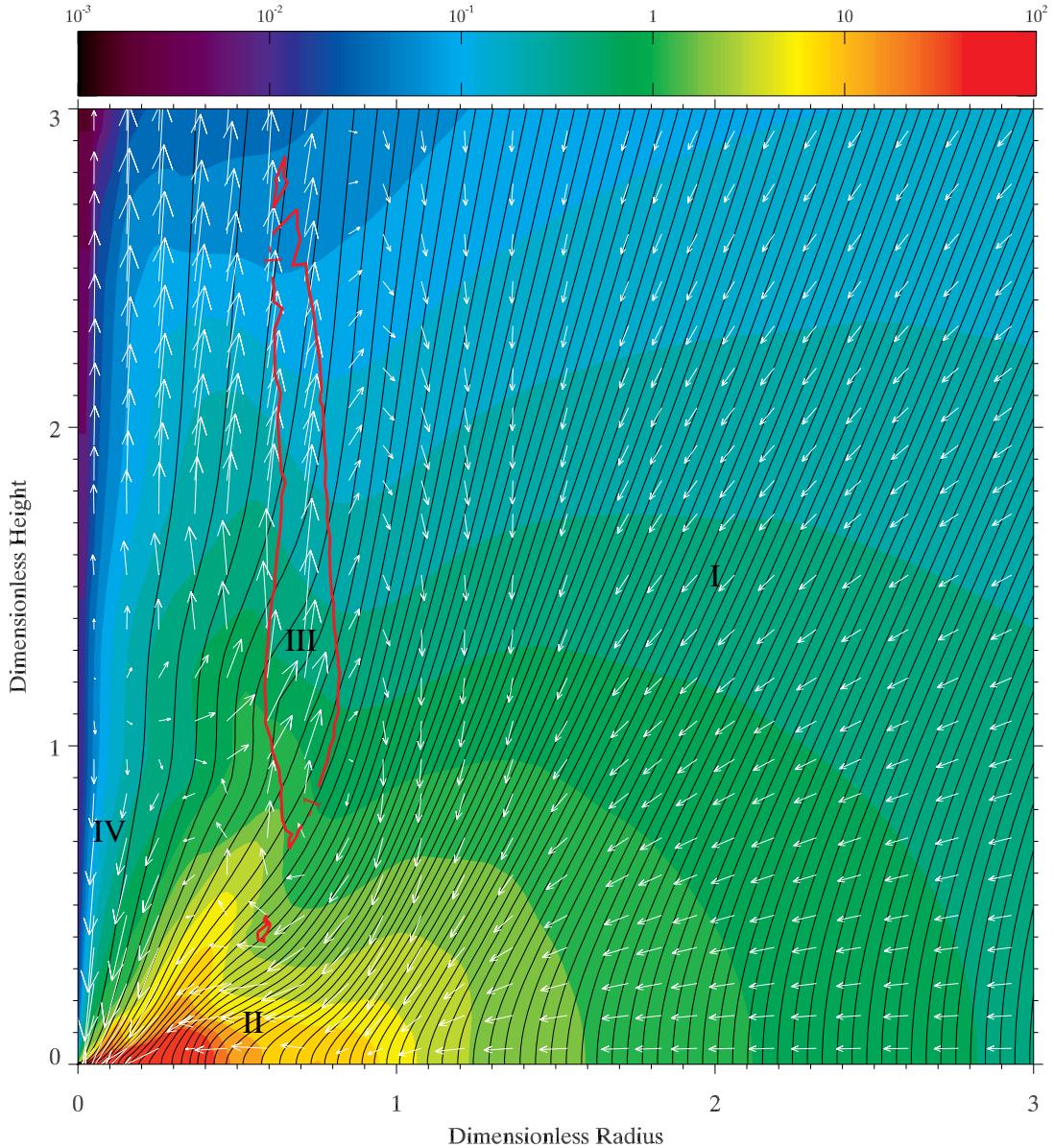
Fig. 15.— Snapshot of the strongly magnetized ($\lambda = 4$) core representative of the state before a "reconnection" event. It is to be compared with the standard case shown in Fig. 2. Enclosed within the red contour is the region where the magnetic field is dominated by the toroidal component. The four dynamically distinct regions are labelled here as in Fig. 2.
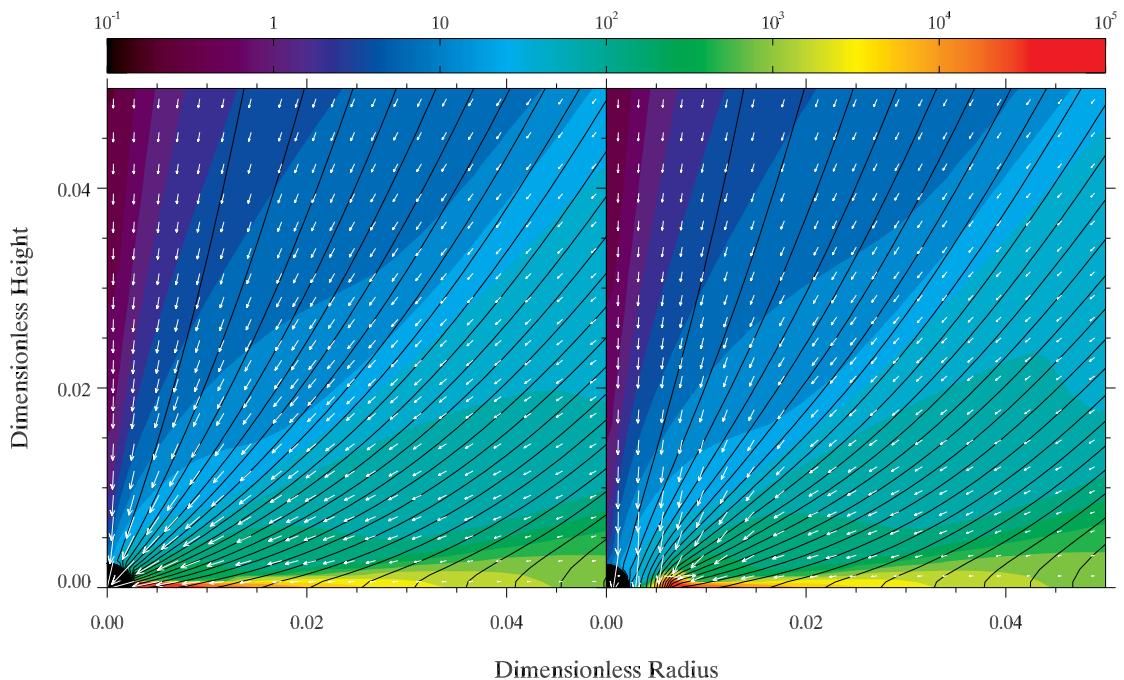
Fig. 16.— Density distribution (color map), velocity field (white arrows) and magnetic field lines (black lines) before (left panel) and after (right) a reconnection event.
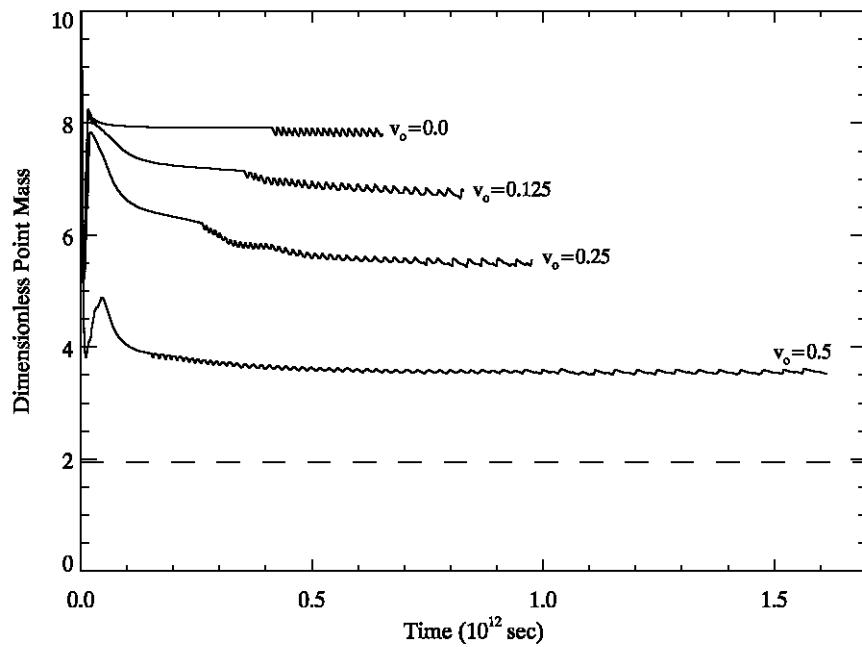
Fig. 17.— Dimensionless central point masses for collapsing cores of the same initial magnetic field ($\lambda = 13.3$) but different rotation speeds. The accretion rate decreases as the rotation rate increases. Also plotted for comparison is the point mass for SIS (dashed line).
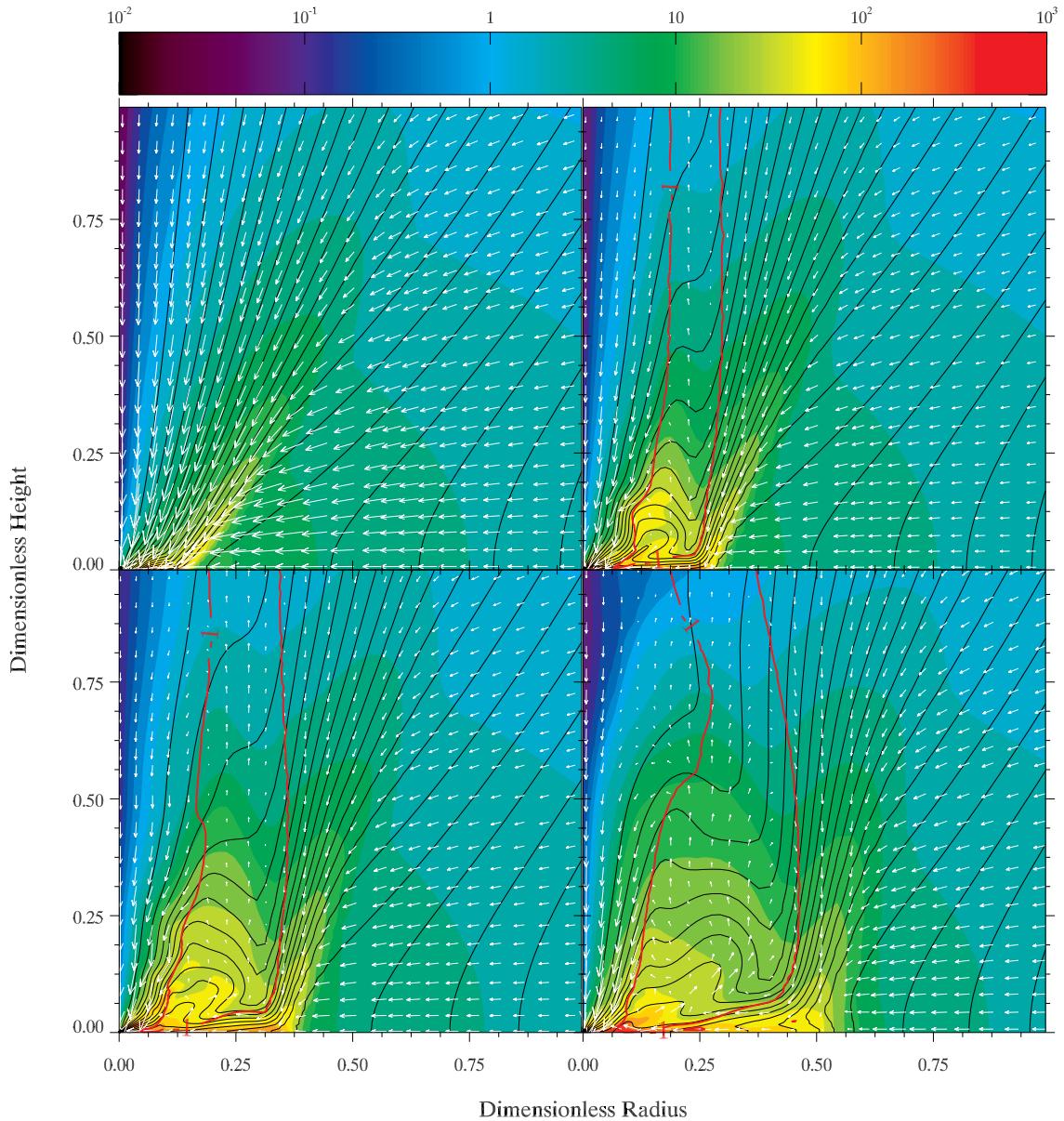
Fig. 18.— Snapshots of collapsing cores of the same initial magnetic field but different rotation speeds of $v_o = 0$ (upper left panel), 0.125 (upper right), 0.25 (lower left), 0.5 (lower right). The magnetic bubble, enclosed within the red contour, becomes thinner with less rotation, disappearing entirely in the non-rotating case.
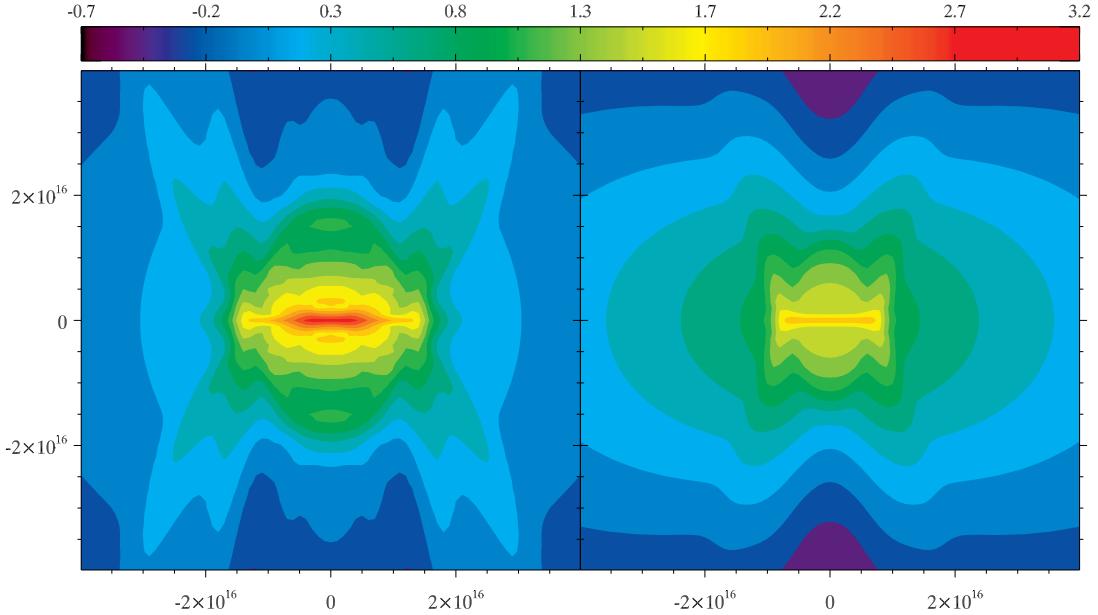
Fig. 19.— Column density distributions for the $\lambda = 80$ case at $t = 2 \times 10^{12}$ sec (left panel) and the $\lambda = 13.3$ case at $t = 8.3 \times 10^{11}$ sec (right) case viewed perpendicular to the axis. In each case, a dense equatorial pseudodisk is surrounded by an extended structure supported by a combination of magnetic fields and rotation — a magnetogyrosphere. The length and column density are in units of $cm$ and $g$ $cm^{-2}$ respectively.
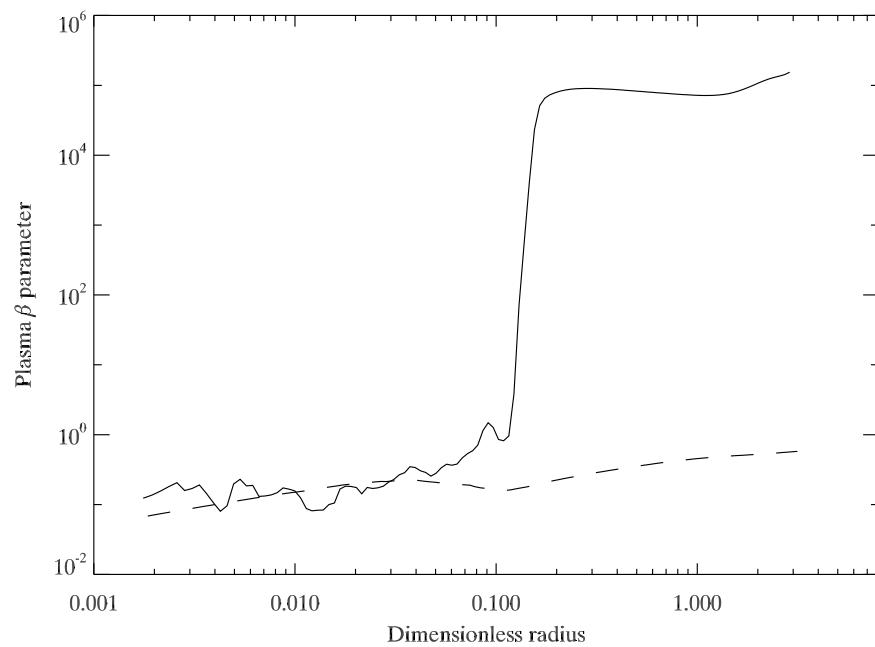
Fig. 20.— Plasma-$\beta$ parameter along a direction $3°$ away from the midplane at a representative time $t = 2 \times 10^{12}$ sec (solid line). Plotted for comparison is a plausible limiting value estimated analytically (dashed line). See text for discussion.